Available online at www.sciencedirect.com
SCIENCE DIRECT®
International Journal of Heat and Mass Transfer 47 (2004) 2293–2316
International Journal of HEAT and MASS TRANSFER
www.elsevier.com/locate/ijhmt

Dynamic response of a capillary pumped loop subjected to various heat load transients

E. Pouzet [a], J.-L. Joly [a,*], V. Platel [b], J.-Y. Grandpeix [c], C. Butto [a]

[a] *Laboratoire Etude des Systèmes et Environnement Thermique de l'Homme (LESETH), Université Paul Sabatier, 118, route de Narbonne, 31062 Toulouse Cedex, France*

[b] *Laboratoire Etude des Systèmes et Environnement Thermique de l'Homme (LESETH), 1, rue de Lautréamont, BP 1624, 65016 Tarbes Cedex, France*

[c] *Laboratoire de Météorologie Dynamique, case courrier 99, Tour 25, 4, Place Jussieu, 75252 Paris Cedex 05, France*

Received 7 December 2001; received in revised form 30 October 2003

Abstract

An experimental capillary pumped loop (CPL) device has been developed in order to study its fundamental response mechanisms following steps of applied power. A global model including all the loop elements and the essential physical processes has been designed, with a sole control parameter for fitting experiments and simulations. By comparing experimental results and simulations for upward and downward steps of heat load, the response mechanisms within the loop can be analyzed. This analysis has revealed a particularly good agreement for damped oscillations of low frequency observed during the undershoots; it also provides an explanation as to the two-phase loop reacts badly to abrupt decreases of applied power.

1. Introduction

Capillary pumped loops (CPLs) and loop heat pipes (LHPs) are two similar types of two-phase systems for extraction and transport of heat. These devices utilize the vapor-liquid phase change to transfer large amounts of heat over long distances between an evaporator and a condenser, in a quasi-isothermal way. CPLs and LHPs are passive devices that need no mechanical pumping: they use the capillary forces of liquid/vapor menisci that are formed at the vicinity of the porous wick surface in order to circulate the fluid and transport heat. Unlike conventional heat pipes, they require only a small heat load to start-up and generate no unwanted vibrations. Both CPL and LHP devices have the same basic operating principle, but the two-phase reservoir is located and connected differently from the rest of the loop.

The first capillary pumped loop (CPL) was developed at the end of the 1960s by Stenger at the NASA Lewis Research Center, where numerous low gravity experiments were came out on board STS shuttles. The first was the capillary pumped loop GAS experiment (G-471), in 1985. A series of on-board experiments called CApillary Pumped Loop (CAPL) were then conducted (1994–1995) in order to test and develop a starter pump designed to clear the vapor lines of liquid prior to CPL evaporator start-up. In 1996, the visualization in an experimental water capillary pumped loop (VIEW-CPL) experiment was carried out in flight; this test loop was designed to investigate the failure of CPLs at low gravity. Finally, the two-phase flow (TPF) experiment, designed to solve problems encountered during the CAPL experiments, was carried out on STS-85 during the TAS mission (1997). The TPF experiment incorporated a new type of starter pump as well as a "capillary flow valve". A review of these NASA experiments and of their main results and features can be found in [1]. All these prototypes were based on the capillary pumped loop concept (CPL) [2]. Another closely related technology, the loop heat pipe (LHP), was invented and first tested in the former Soviet Union by Maidanik et al. [3]. This concept, adopted by the main US companies

* Corresponding author.
E-mail address: jlj@sphinx.ups-tlse.fr (J.-L. Joly).

0017-9310/$ - see front matter © 2003 Elsevier Ltd. All rights reserved.
doi:10.1016/j.ijheatmasstransfer.2003.11.003

Nomenclature

Symbol, definition, SI units

a	accomodation factor in Langmuir law
c	specific heat at constant pressure, $J\,kg^{-1}\,K^{-1}$
D	diameter, m
e	thickness, m
F	force, N
g	gravitationnal acceleration, ms^{-2}
h	heat transfer coefficient at the liquid–vapor interface, $W\,m^{-2}\,K^{-1}$; specific enthalpy of liquid, $J\,kg^{-1}$
H	height, m
k	characteristic microroughness size, m or thermal conductivity, $W\,m^{-1}\,K^{-1}$
l_v	latent heat of vaporization, $J\,kg^{-1}$
L	length, m
$\dot{m}$	mass flow rate, $kg\,s^{-1}$
M	molecular weight, $kg\,mol^{-1}$
p	pressure, Pa
p_l^*	liquid pressure under menisci, Pa
Pe	Peclet number
r	radius, meniscus curvature radius, m or gas constant, $J\,kg^{-1}\,K^{-1}$
R	universal gas constant, $J\,mol^{-1}\,K^{-1}$
Re	Reynolds number
S	area, m^2 or cross-sectional area, m^2
S_w	outer surface of wick, m^2
t	time, s
T	temperature, K or °C
v	axial velocity, $m\,s^{-1}$
x	axial coordinate, m

Greek symbols

α	vapor void fraction
β	liquid zone length in the condenser, m
ΔH	elevation difference, m
Δp	pressure difference, $N\,m^{-2}$
ε	wick porosity
η	two-phase zone length in the condenser, m
θ	inclination angle from vertical, rad
ρ	density, $kg\,m^{-3}$
ρ^+	density ratio ρ_v/ρ_l
κ	permeability, m^2
λ	friction factor coefficient
μ	dynamic viscosity, $N\,m^{-2}\,s$
Σ	liquid–wick contact area, m^2
σ	surface tension of working fluid, $N\,m^{-1}$
τ	characteristic time, s
ϕ	heat rate, W
φ	heat flux, $W\,m^{-2}$
Ω	control volume, m^3
ξ	dimensionless axial coordinate

Subscripts

c	condenser
cap	capillary
cs	at the interface between liquid in the condenser and countercurrent secondary flow
e	evaporator
g	groove
h	hydraulic
i	insulator
,i	inlet
I	interface
la	at the interface between liquid in lines and ambient air
lw	at the interface between liquid and wick porous structure
l	liquid
o	outlet
r	reservoir
rT	between reservoir and tee-connexion
s	jacket solid wall
sat	saturation
t	relative to thermostated bath
tr	at interface between thermostated bath and reservoir
v	vapor
w	porous wick structure
η	end of two-phase zone at the condenser
0	at reference state

Superscripts

·	time derivative
–	averaged value
*	liquid–vapor interface

(Thermacore and Dynatherm) is nowadays under full development. A review of the characteristics and the differences between both systems can be found in [4,5]. Finally, the Europeans tested their own device in 1993 [6], and new prototypes will next be tested during the future flight of the Stentor satellite.

In the recent developments in the space industry (increase in dissipated powers particularly in telecommunications satellites [7], development of orbiting space stations, etc.), the generic capillary loops are emerging as state-of-the-art technological designs for thermal control of future spacecraft. Today, such capillary loops are becoming available for practical use and are tested to provide thermal control in satellites such as the Earth Observing System, the Hubble Space Telescope, the Mars Surveyor [8], or the French demonstrator satellite Stentor.

Both CPL and LHP technologies have reached a high level of sophistication and their behavior and characteristics in steady state are well known. Their only weak point remains the presence of permanent pressure oscillations, at high frequencies. These oscillations, first reported by Ku, have been intensely investigated; they are accepted as a phenomenon inherent to the capillary loops operation [9]. This is why many recent works have been dedicated to the study of transient regimes, and to the more or less unstable behavior that the system can present during the starting up or in response to the application of power cycles to the evaporator surface. It is well known in the case of the CPLs that in certain starting up conditions or as a reaction to a significant fall of applied power, unstable mechanisms may potentially cause the dry-out of the evaporator and the subsequent rapid system failure.

As regards the start-up failures, all experiments on CPL have demonstrated that large pressure oscillations preceded the process of deprime in the evaporator. For want of a better means of controlling this insuitable behavior, CPLs usually use an auxiliary starter pump [10].

The fundamental mechanisms responsible for this unstable behavior have not been clearly identified; the presence of the three free liquid/vapor interfaces does indeed entail the generation of hydrodynamic instabilities. It seems that there are several physical mechanisms responsible for the onset of these instabilities. Combined together, they can lead eventually to extreme situations such as the dry-out of the evaporator. Investigations have thus been carried out in order to study the primary mechanisms which can generate pressure oscillations. The works of Figus et al. [11], Liao and Zhao [12] and Zhao and Liao [13] have shown that the causes of these oscillations could be connected to the instabilities of menisci located in the vicinity of the porous structure surface. It has also been shown that the presence of bends in the long transport lines of the loop (and in particular at the evaporator outlet) can lead to liquid bridging which adds to the high frequency pressure oscillations [14]. Among the supposed causes described above, no mechanism can be considered as solely responsible for the global unstable behavior during start-up or after an abrupt loss of applied power. It is also necessary to look at how the couplings work in the system as a whole, for an explanation of the process of development of these intrinsic instabilities. Combined with sudden variations of applied external conditions, these instabilities end in a system failure. Another point of concern is the interaction mechanisms between the control reservoir and the rest of the CPL loop, that can amplify the high frequency oscillations in the pumping pressure.

It is important to study the behavior of the CPLs in response to the demands of the control parameters, particularly that of the applied power. Our understanding of the mechanisms leading to deprime of the evaporator cannot easily be improved by experiments alone, especially if these experiments uncouple the loop components. Valuable help comes from investigations by means of numerical CPL models at the system level. Modelling designs initially focused on the evaporator behavior, considered as essential. First, numerical models described separately the role of the porous material [15] or of the heating jacket [16]. Cao and Faghri [17] then modeled the porous material and heating body taken as a single unit. Demidov and Yatsenko [18] have coupled it to the vaporization mechanism of the fluid at the saturated wick surface. Finally, a numerical model which also integrated the influence of the drainage of vapor into grooves was designed by Cao and Faghri [19]. However, these works, limited to the mechanisms acting on the evaporator component, showed that more and more global models were indispensable for understanding of the behavior of the device as a whole. On the other hand, simple global models, based on the energy balance and/or the pressure losses yield the stationary characteristics and the limits of the operation at steady state; they also provide heat and mass transfers. But they are of no help in interpreting the transient mechanisms of oscillation development. There are few complete CPL models allowing for an analysis of these mechanisms. A nodal CPL model describing the transient temperature and pressure variations, has been proposed by Schweickart et al. [20] and compared with experimental data. The main numerical difficulties seem to have been the description of the liquid/vapor interface in the condenser, and the need to fit too many parameters into the experiment, which entails a cumbersome calculation process.

The present work aims at studying the mechanisms of development of the unstable behavior during the cyclical functioning of the CPLs. A global loop model has been designed that accurately takes into account the dynamics of the two-phase interface in the condenser and in the reservoir. The modelling of the condenser is based on the results of Bhatt and Wedekind [21] who base their condenser model on the main hypothesis of constant void fraction. This has enabled to build a model whose main quality is to describe accurately the dynamic behavior of the two-phase interface in the condenser.

The present numerical model provides a satisfactory reproduction of the CPL response after steps up and down of applied power. In comparison with experimental data, the low frequency damped oscillations accompanying the undershoot effects are particularly accurate. An analysis of mechanisms coupled between the reservoir and the rest of the loop during these phases has been made, highlighting the effect of the couplings of physical phenomena and of the interactions between loop components. A specific simulation makes

it possible to explain the coupled mechanisms leading to the evaporator deprime, when the power step down is too great.

2. Operating principle

A schematic diagram of our experimental setup is shown in Fig. 1. The test bench used to obtain the measurements presented here includes two evaporators in parallel, which can work separately or simultaneously, a condenser and a control reservoir, with a thermally controlled tank to provide accurate temperature controls.

Capillary pumping is the driving force of the device and it takes place within a porous medium in the form of a hollow tube with one end closed (Fig. 2). The liquid arrives in the tube and, by capillary action, crosses the wick to reach the outside surface of the tube where it vaporizes, thus creating menisci at the wick surface. The porous tube is fitted into a hollow metal cylinder (the evaporator jacket) containing longitudinal grooves on its internal surface which allow the vapor to evacuate towards the vapor line and play an important role at the onset of boiling.

The condenser has to ensure total condensation of the vapor, evacuating the resulting heat, and also allowing the liquid to be subcooled by a few degrees to prevent the presence of vapor bubbles during the fluid return to the evaporator.

The control reservoir has the peculiarity of containing a large amount of the working fluid and having a free liquid–vapor interface in thermodynamic equilibrium. Its role is to fix the loop setpoint at steady regime (p_r^*, T_r^*), which makes it the decisive control organ of the loop. It is connected to the liquid line by a short pipe. The location of the reservoir relative to the two essential components of the loop (evaporator, condenser) has very important consequences on the system operating conditions. Being strongly coupled to the condenser (as the data and the analysis of the results from the numerical model show [22]), the reservoir acts as a

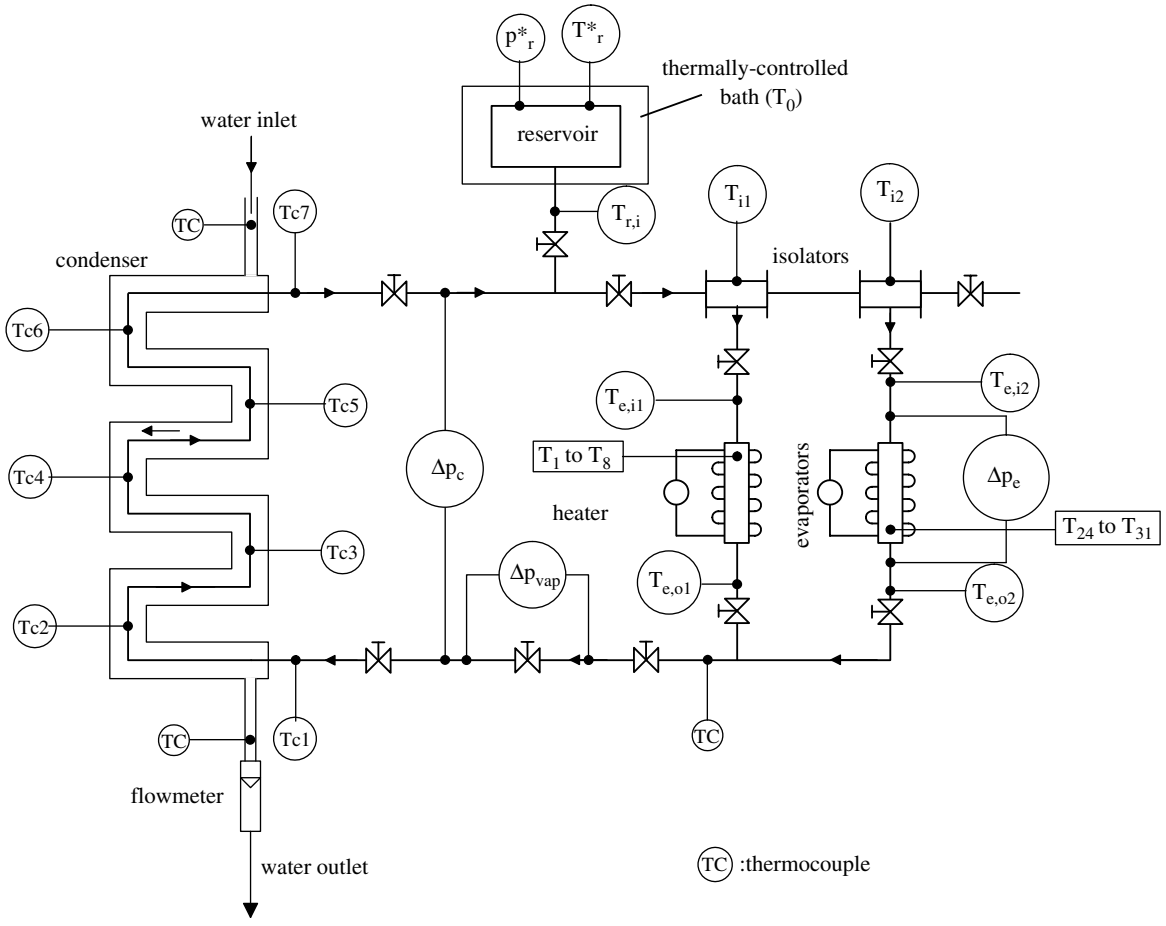

Fig. 1. Schematic of the CPL device.

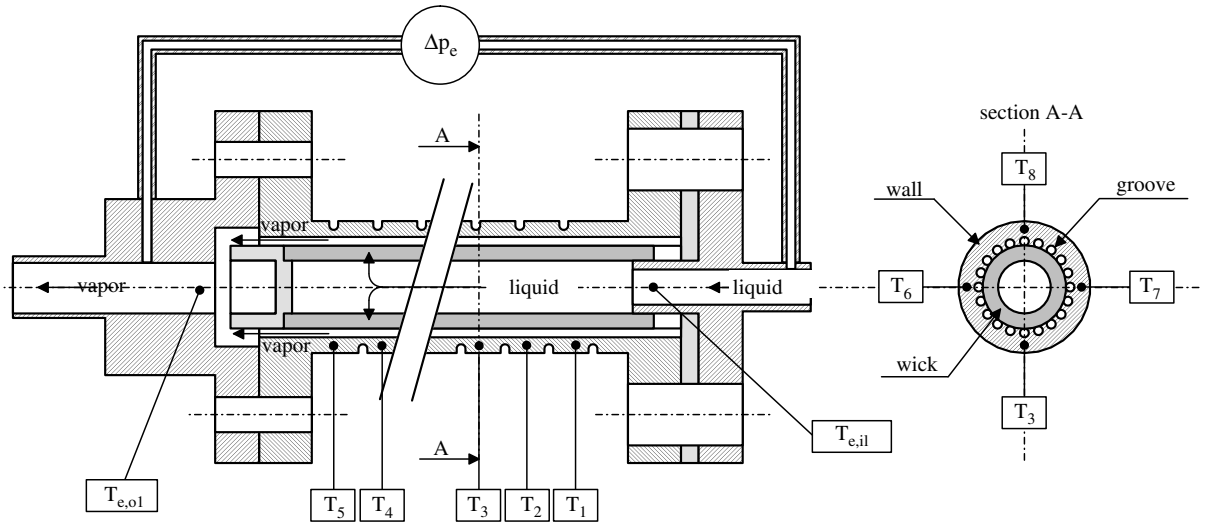

Fig. 2. Schematic of the evaporator.

powerful damper once steady running is established, especially during variations in the heat load applied to the evaporator or recovered by the condenser. The thermal inertia of the reservoir, combined with the mechanical inertia of the liquid which constantly exchanges with the loop, are the fundamental features by which the reservoir influences loop behavior. It intervenes, on the one hand, by imposing an operating pressure where it is connected to the loop and, on the other hand, by continually exchanging liquid with the loop. Any addition or removal of liquid in the reservoir is revealed by phase transitions and by heat transfers, first within the fluid and then between the reservoir and the thermally controlled tank. These two aspects of its role are completely coupled through the complex dynamics which are developed with the rest of the loop.

The insulator is an element, placed upstream from the evaporators, which plays a dual role. On the one hand, it traps non-condensable gases and vapor bubbles transported by the liquid flow, which could provoke capillary pumping drainage by obstructing the evaporator wick. On the other hand, if the wick of one of evaporators dries out as a result of a too large heat load, the vapor could flow back from the evaporator to the insulator. The menisci that then form at the insulator wick surface could block the vapor flow and prevent it from propagating and draining the other evaporators.

One of the main limitations of the system is the capillary pressure drops (which depends on both the thermophysical properties of the working fluid and the characteristics of the porous wick). It is therefore imperative to minimize the pressure drops during device design. The choice of diameters for the transport lines is also important. Numerous valves have been arranged around the whole loop to control the flows or simulate pressure drop variations.

3. Test loop design

All the components of the test device (Fig. 1) are arranged on the same horizontal level, defined by the free liquid/vapor interface in the reservoir. This configuration is necessary to minimize effects of gravity. By means of a rack and pinion device, it is possible to move the condenser plane vertically with regard to the evaporator plane. The two parallel evaporators have been arranged on a same plane.

3.1. Cylindrical evaporator (Fig. 2)

The cylindrical evaporator body is made of fortal (aluminum alloy), a material possessing good heat conduction properties. There are 20 longitudinal grooves, 2 mm in diameter, on its inside surface, in which the vapor circulates. The surface in contact with the porous wick (polyethylene wick of minimum pore size of 10–15 μm) has circular striations 0.1 mm deep in order to intensify vapor evacuation. The studies carried out show that this striation improves the interface heat transfer coefficient by a factor of 2 relative to a smooth contact area [23].

Each evaporator may be warmed independently on its outer surface by a spiral wire resistor providing to 600 W (corresponding to a maximum heat flux of about 5 $W\,cm^{-2}$ at the porous wick surface).

The evaporator was instrumented by 10 chromel–alumel (K-type) thermocouples arranged at mid-diameter on

each evaporator. The response time of these thermocouples is estimated at 3–4 s and the acquisition frequency is 1 Hz, which ensures a good signal resolution. Two thermocouples give the liquid temperature at the evaporator inlet ($T_{e,i1}$ or $T_{e,i2}$) and two others the vapor temperature at the outlet ($T_{e,o1}$ or $T_{e,o2}$; see Fig. 2). Five more measure the temperature along the cylinder (thermocouples T_1 to T_5); and another three measure the temperature at diametrically opposite locations of the median plane of the cross-section A–A (thermocouples T_3 to T_8). The metal body temperature of each evaporator is determined by means of averaging the values measured by these thermocouples.

The pressure difference Δp_e between the liquid and vapor phases at the evaporator inlet and outlet was measured by a differential pressure transducer. This sensor is accurate to within ±12.5 Pa according to the manufacturer. This measurement requires great care as it was taken between two zones where the fluid was in different states (liquid and vapor).

3.2. Condenser

This component is composed of two concentric tubes, arranged on a plane. The working fluid circulates in a copper inner tube, whose external fins are in contact with the countercurrent cooling water. The condenser length was oversized, in order to ensure efficient liquid subcooling.

Seven thermocouples (T_{c1} to T_{c7}), arranged at meter intervals (Fig. 1), measure the working fluid temperatures, thus providing a rough estimate of the length over which two phases were present. Two thermocouples were located at the inlet and the outlet of the cooling secondary circuit and give the two temperatures respectively. Taken with the flowmeter reading, they enable the thermal power recovered by the condenser to be estimated. The pressure difference $\Delta p_c = p_{c,i} - p_{c,o}$ between condenser ends was measured by a differential pressure transducer.

3.3. Control reservoir

The 2.5 l reservoir is composed of a horizontal cylindrical steel shell in thermal equilibrium immersed in a thermostated water bath. A transparent window in a line allows the liquid height in the reservoir to be visualized at any time.

A K-type thermocouple of approximately 0.5 mm weld size, was placed in the working fluid flow and measures the liquid temperature $T_{r,i}$ at the reservoir inlet (Fig. 1). The same type of thermocouple measures the vapor-phase temperature T_r^* in the reservoir. An absolute pressure sensor measures the vapor pressure p_r^* in the reservoir with an accuracy of ±250 Pa.

3.4. Insulator

The insulator contains a porous body that the liquid has to cross before reaching the evaporator. Two thermocouples (Fig. 1) measure the temperature of the working fluid in the insulators T_{i1} and T_{i2}.

3.5. Liquid and vapor lines

The lines are made of copper and are thermally insulated. Elbows, joints and valves were inserted in such a way to minimize the pressure losses as far as possible. An artificial pressure drop Δp_{vap} is created by means of a valve placed on the vapor line allowing simulating very long pipes pressure loss (Fig. 1).

The fluid HFC-134a (CH_2FCF_3) was chosen as the working fluid.

The main geometrical characteristics of each of the elements composing the loop are given in Appendix A.

4. Model of the complete loop

The model of the complete loop is designed to identify and to analyze the main physical phenomena which come into play in the functioning of these devices in order to control them better.

Because of the strongly coupled physical mechanisms acting in such a system, our modelling approach consists in simplifying the most geometrically or technologically complex elements while retaining as far as possible the main physical phenomena responsible for the behavior of capillary loops. The simplifications and the hypotheses selected will be examined in detail when the equations governing the behavior of each of these components are reviewed.

In pursuing such an approach, it must further be noticed that the description levels go from elementary scale submodels such as the vaporization interface to global scale submodels, e.g. for the two-phase mechanisms acting in the condenser. These submodels (in the form of balance equations or transfer laws) are then linked in a modular way to form the global loop model. The numerical model is then composed as an appropriate description using transfer evolution formalism (TEF) and the simulations are carried out by the ZOOM software [24].

The global model shown below is broken down into coupled main submodels, corresponding to each type of loop component: evaporator, vapor line, condenser, liquid lines and reservoir (Fig. 3).

4.1. Evaporator model

As we have seen, the evaporator is composed of a cylindrical metal pipe with longitudinal grooves which

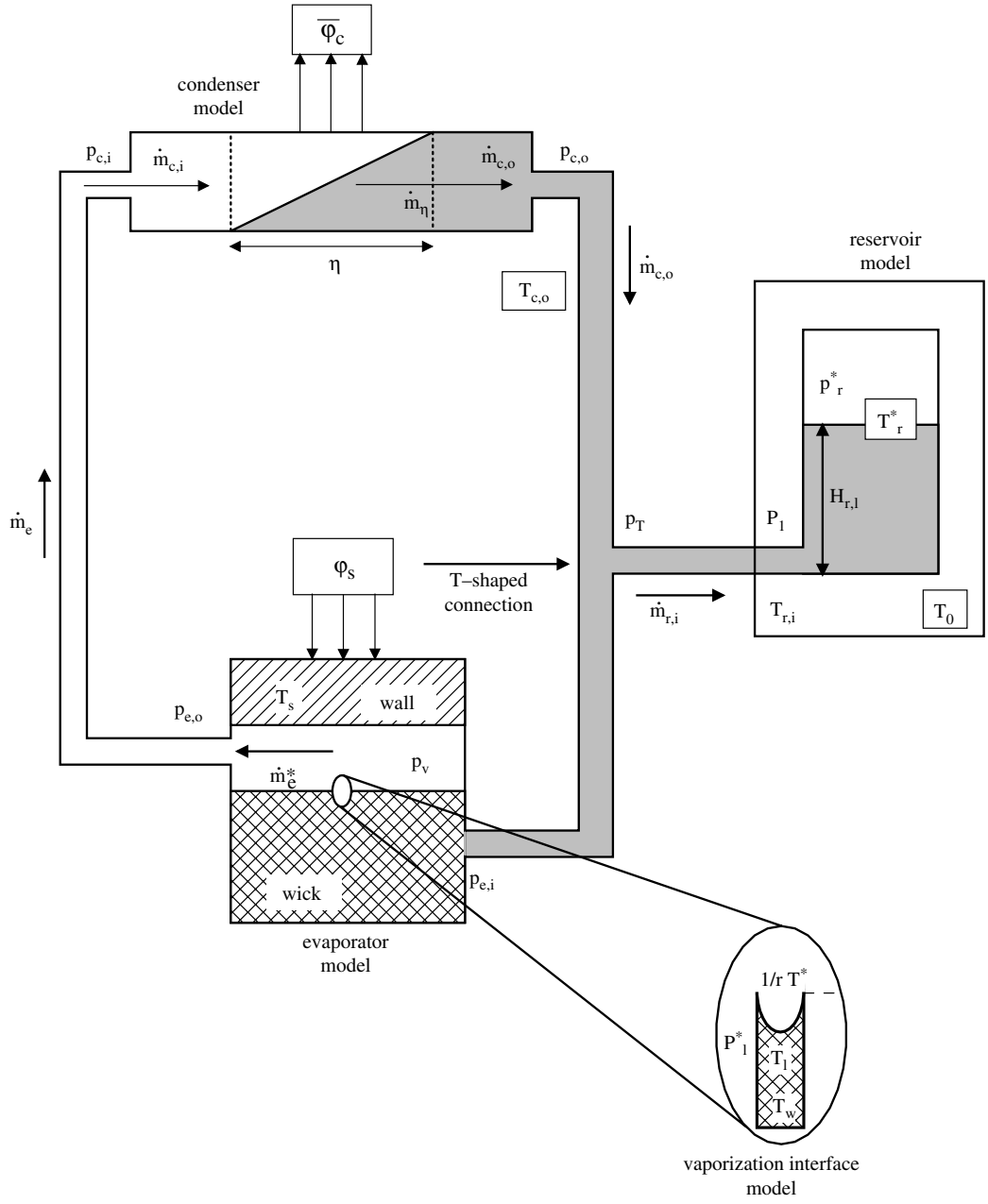

Fig. 3. Loop schematic showing the variables of the model.

hold a porous wick in such a way as to optimize the thermal exchanges. The heat to be evacuated towards the cold sink is transferred by conduction through the massive pipe jacket to the wick surface. The liquid arrives directly along the wick axis. It then progresses radially by capillary pumping until it reaches the external surface of the wick, thus saturating it. Upon contact with the warm metal elements, the liquid vaporizes; the vapor is then collected and channelled towards the vapor line through grooves. The porous wick plays a major role in bringing the liquid into the zone where it is vaporized without slowing its progress and without allowing thermally insulating vapor bubbles to form, which would block the arrival of liquid and lead to loop drainage. As regards the flow of fluid in the wick, it is described by a laminar Darcy flow, valid for the sintered structure of the porous medium (the permeability value 1.1×10^{-12} m^2 was measured in the

laboratory). Heat conduction within the wick is taken into account.

From this brief description of the processes, let us now begin by describing the processes crucial for loop operation which are situated at the vaporization interface.

4.1.1. Models of the physical processes operating at the vaporization interface

The zone where the liquid vaporizes in the space confined between the heating jacket and the porous wick and which leads out into the grooves is a crucial subdomain for the operation of the evaporator and the whole loop.

If we accept the hypothesis that the vaporization interface is able to adapt itself instantaneously to the constraints imposed by the rest of the loop, this interface has been considered as being composed of menisci, i.e. curved surfaces without thickness or thermal inertia, localized at the wick surface. For the porous wicks of very weak thermal conductivity and of very low fusion temperature used in space applications, the interface cannot regress deeply into the wick, without risking destruction by fusion, as observed in our device during the setting up phase. Vaporization entails a disappearance of liquid (and creation of menisci) which causes two fundamental mechanisms to come into action: pumping of the liquid and expulsion of the vapor towards the condenser.

(1) The capillary forces $F = 2\pi\sigma\bar{r}$ maintain the liquid–vapor interface at the wick top.
(2) The capillary pressure drop $\Delta p_{\mathrm{cap}} = p_{\mathrm{v}} - p_{\mathrm{l}}^{*} = 2\sigma/\bar{r}$ between the two sides of the meniscus is the system's driving mechanism (Young–Laplace law).

These mechanisms are the mainspring of evaporator dynamics. Vaporization and capillary effects act in phase to keep the global mass flowrate $\dot{m}$ in the loop constant. Otherwise oscillations are observed.

With these hypotheses, the balance equations show that the interface variation can be characterized by only two state variables [25]: the meniscus curvature and the interface temperature.

• Assuming that the mass flowrate produced in the vaporization interface is given by Langmuir's law,

$$\dot{m}^{*} = \varepsilon S_{\mathrm{w}} \sqrt{\frac{M}{2\pi R T^{*}}} \left(a_{\mathrm{e}} p_{\mathrm{sat}}(T^{*}) - a_{\mathrm{c}} p_{\mathrm{v}}\right) \tag{1}$$

and that the thermodynamic equilibrium conditions for a hemispherical liquid–vapor interface obey, to the first order:

$$p_{\mathrm{sat}}\left(T^{*}, \frac{1}{\bar{r}}\right) = p_{\mathrm{sat}}\left(T^{*}, \frac{1}{\bar{r}} \to 0\right) - \frac{2\sigma}{\bar{r}} \frac{\rho_{\mathrm{v}}}{(\rho_{\mathrm{l}} - \rho_{\mathrm{v}})} \tag{2}$$

it can be shown that the average curvature of the menisci is a function of the vaporization interface temperature T^{*}, the vapor pressure p_{v} and the liquid speed v_{l}^{*} at the vaporization interface:

$$\frac{1}{\bar{r}} = \frac{1}{2\sigma} \left\{ \underbrace{\frac{(\rho_{\mathrm{l}} - \rho_{\mathrm{v}})}{\rho_{\mathrm{v}}} \left[p_0 \mathrm{e}^{\left[-\frac{M l_{\mathrm{v}}}{R} \left(\frac{1}{T^{*}} - \frac{1}{T_0} \right) \right]} - \frac{a_{\mathrm{c}} p_{\mathrm{v}}}{a_{\mathrm{e}}} \right]}_{[\mathrm{A}]} - \underbrace{(\rho_{\mathrm{l}} - \rho_{\mathrm{v}}) \frac{\rho_{\mathrm{l}}}{\rho_{\mathrm{v}}} \frac{1}{a_{\mathrm{e}}} \sqrt{\frac{2\pi R T^{*}}{M}} v_{\mathrm{l}}^{*}}_{[\mathrm{B}]} \right\} \tag{3}$$

where $p_0 = p_{\mathrm{sat}}(T_0)$ is the saturated vapor pressure known from reference temperature T_0.

It is necessary to note the presence of two terms with opposite effects:

- Contribution [A] expresses the kinetics of vaporization for an interface at temperature T^{*} in contact with a vapor phase at pressure p_{v}, and so increases the meniscus curvature downwards,
- Contribution [B] couples the liquid dynamics v_{l} with the interface thermal behavior T^{*} and means that any injection of liquid pumped by a "mean capillary tube" helps to decrease the meniscus curvature.

In fact, we are going to chart the changes in pressure p_{l}^{*} under the meniscus, i.e. immediately under the vaporization interface. We shall rewrite the last equation, using the Young–Laplace law, in the form of a non-linear implicit equation expressing p_{l}^{*} according to the state variables which are instantaneously connected with it:

$$p_{\mathrm{l}}^{*} = f\left(T^{*}, p_{\mathrm{v}}, v_{\mathrm{l}}^{*}\right) \tag{4}$$

One of the reasons for this choice is to have a state variable determined by the model that allows device malfunctions to be detected. As the meniscus curvature has a maximum allowed value, Δp_{cap} cannot exceed a certain threshold, otherwise the interface would irreversibly move back into the wick and the evaporator would dry out. This explains the importance for the analysis of charting the observable pressure p_{l}^{*}.

• As regards the vaporization interface temperature, the balance equation of heat becomes established by means of the following stages [25].

The First Law of Thermodynamics is applied to an elementary control volume containing liquid and vapor zones around the evaporation interface. Supposing that the saturated fluid is isothermal and that the exchanged heat contributes only to the evaporation and to the

variation of kinetic energy, the following equation can be derived:

$$\dot{m}\left[\left(h_{\mathrm{v}}+\frac{1}{2}v_{\mathrm{v}}^2\right)-\left(h_{\mathrm{l}}+\frac{1}{2}v_{\mathrm{l}}^2\right)\right] = \dot{m}\left[l_{\mathrm{v}}+\frac{1}{2}\left(v_{\mathrm{v}}^2-v_{\mathrm{l}}^2\right)\right]=\varphi^* \tag{5}$$

It is also assumed that the energy involved during the deformation of menisci and the working of the friction forces are insignificant compared to the variation of total energy of the control volume. For this control volume representative of the zone of evaporation, the heat balance can be written:

$$\varphi^*=\varphi_{\mathrm{s}}+\varphi_{\mathrm{l}}+\varphi_{\mathrm{w}} \tag{6}$$

$$=h^*S^*(T_{\mathrm{s}}-T^*)-\varepsilon k_{\mathrm{l}}\frac{\partial T_{\mathrm{l}}}{\partial z}\Bigg|^* + \dot{m}S^*c_{\mathrm{l}_{T^*}}T^*-(1-\varepsilon)k_{\mathrm{w}}S^*\frac{\partial T_{\mathrm{w}}}{\partial z}\Bigg|^* \tag{7}$$

with $\dot{m}=\dot{m}_{\mathrm{v}}=-\dot{m}_{\mathrm{l}}$.

By combining the relations (5) and (6), after discretization, the following formal expression for T^* can be obtained [25]:

$$T^*=\frac{h^*T_{\mathrm{s}}+\varepsilon(h_{\mathrm{l}}+\rho_{\mathrm{l}}c_{\mathrm{l}}v_{\mathrm{l}})T_{\mathrm{l}}+(1-\varepsilon)h_{\mathrm{lw}}T_{\mathrm{w}}-\varepsilon\rho_{\mathrm{l}}v_{\mathrm{l}}^*\left(l_{\mathrm{v}}+\frac{1}{2}\left(v_{\mathrm{v}}^2-v_{\mathrm{l}}^2\right)\right)}{h^*+\varepsilon h_{\mathrm{l}}+(1-\varepsilon)h_{\mathrm{lw}}+\varepsilon\rho_{\mathrm{l}}c_{\mathrm{l}}v_{\mathrm{l}}^*} \tag{8}$$

4.1.2. Thermal and dynamic variation of the liquid in the wick

The heating jacket is discretized into cylindrical sectors (i,j) of radius r_i and inclination angle from vertical θ_j. This allows the transient temperature profile and the heat fluxes crossing the jacket to be obtained.

In the same way, the wick saturated with liquid is discretized into cylindrical sectors (i,j). This yields the local liquid temperature T_{l}, and the local wick temperature T_{w}.

For a mesh element (i,j) bounded radially by two interfaces (I,j) and $(I+1,j)$ and by two interfaces (i,J) and $(i,J+1)$ according to the angular orientation, the thermal balance equations are for both solid wick and liquid sectors:

$$\begin{cases}\rho_{\mathrm{l}}L_{\mathrm{l}}\varepsilon\Omega_{i,j}\frac{\partial T_{\mathrm{l}_{i,j}}}{\partial t}=\sum_{I,J}\phi_{\mathrm{l}_{I\text{ or }J}}+h_{\mathrm{lw}}\Sigma(T_{\mathrm{w}_{i,j}}-T_{\mathrm{l}_{i,j}})\\ \rho_{\mathrm{w}}L_{\mathrm{w}}(1-\varepsilon)\Omega_{i,j}\frac{\partial T_{\mathrm{w}_{i,j}}}{\partial t}=\sum_{I,J}\phi_{\mathrm{w}_{I,J}}-h_{\mathrm{lw}}\Sigma(T_{\mathrm{w}_{i,j}}-T_{\mathrm{l}_{i,j}})\end{cases} \tag{9}$$

with, for example, for a radial conductive heat transfer at interface (I,j) of radial position r_I and angular position θ_j:

$$\phi_{\mathrm{l}I,j}=h_{\mathrm{l}_{I,j}}(T_{\mathrm{l}_{i-1,j}}-T_{\mathrm{l}_{i,j}})+\dot{m}_{\mathrm{l}_{I,j}}c_{\mathrm{l}}T_{\mathrm{l}_{I,j}} \tag{10}$$

where $\dot{m}_{\mathrm{l}_{I,j}}$ and $T_{\mathrm{l}_{I,j}}$ are defined at interface (I,j) according to a numerical scheme dependent on the local Peclet number.

The liquid flowrate in a sector (i,j) of the wick verifies, independently of the radial coordinate (i), that:

$$\frac{\partial\dot{m}_{\mathrm{w}_j}}{\partial t}=\frac{1}{1+\pi\frac{L_{\mathrm{e}}}{e_{\mathrm{w}}}\frac{L_{\mathrm{e}}}{S_{\mathrm{c}}}D_{\mathrm{w}_i}}\left(\pi L_{\mathrm{e}}\left(\frac{p_{\mathrm{e},i}D_{\mathrm{w}_i}-p_{\mathrm{l}}^*D_{\mathrm{w},e}}{e_{\mathrm{w}}}\right)-\pi\rho_{\mathrm{l}}g\overline{D}_{\mathrm{w}}L_{\mathrm{e}}\sin\theta_j-\frac{\mu_{\mathrm{l}}}{\rho_{\mathrm{l}}\kappa}\dot{m}_{\mathrm{w}_j}\right) \tag{11}$$

4.1.3. Vapor flow in grooves

Assuming that the vapor flowrate in the grooves increases linearly with groove length L, it can be demonstrated [26] that the vapor pressure drop between the groove ends is related to the resultant flowrate $\dot{m}_{\mathrm{v}}$ in the vapor line by:

$$\Delta p_{\mathrm{g}}=\frac{4^{b+2}aL_{\mathrm{e}}}{2(b+3)\pi^{b+2}D_{\mathrm{hg}}^{b+5}\rho_{\mathrm{v}}\mu_{\mathrm{v}}^b}\dot{m}_{\mathrm{v}}^{b+2} \tag{12}$$

The pair of constants (a,b) depends on the flow regime. For the regimes encountered in our experimental device (laminar and turbulent regimes), these constants values are:

$$\begin{cases}a=64,\ b=-1 & \text{for the laminar regime}\\ a=0.1643,\ b=-0.177 & \text{for the turbulent regime}\end{cases}$$

4.1.4. Thermal and flow couplings between heating jacket, wick and grooves

The above relations (1), (4) and (8) are not sufficient to link the processes occurring at the vaporization interface with those connected to the physical elements which surround it (liquid-saturated wick, metallic elements, etc.). Other transfer laws are needed to complete the first two: the conduction flux laws for φ_{s}^* (between the heating jacket and interface), φ_{l}^* (heat flux between the liquid phase circulating in the wick and the interface) and φ_{w}^* (heat flux between the solid part of the wick and the interface).

4.2. Condenser model

The numerical condenser model used has been developed from the work of Wedekind and co-workers [21,27,28]. The essential part of their hypotheses and initial basic equations have been used, although completely reformulated as to interconnect the numerical condenser model with the other submodels of the

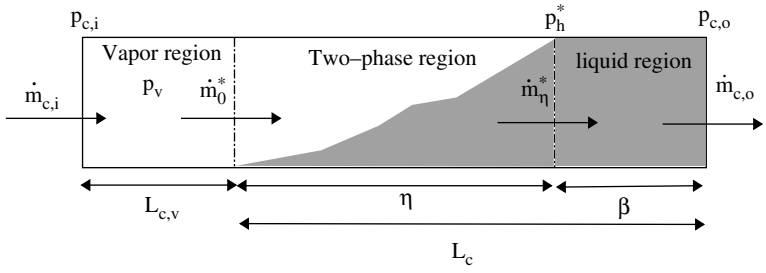

Fig. 4. Variables of condenser model.

complete loop. The numerical model designed by Wedekind offers the advantage of reproducing the global transient behavior of the condenser without requiring geometrical discretization or particular processing of each of the vapor and liquid phases.

Using a 1D hypothesis, it treats only variables globalized over the whole condenser (Fig. 4) and eliminates any stochastic fluctuations during the observation time scale. This is the case for variables such as: condensation zone length $\bar{\eta}(t)$ following the x axial direction, mass flowrates at the inlet $\dot{m}_{c,i}$ and outlet of the condensation zone $\dot{m}^*_\eta$ and at the condenser outlet $\dot{m}_{c,o}$ (flowrates that can be different in the frequently occurring case where the liquid–vapor interface moves rapidly into the condenser), and pressures at the end of the condensation zone p^*_η and at the condenser outlet $p_{c,o}$.

The global aspects of this numerical model can be expressed via the following hypotheses:

(1) The system provides complete condensation, which means that the two-phase zone length $\bar{\eta}(t)$ is finite.
(2) The vapor void fraction $\bar{\alpha}_c$, averaged over the complete two-phase length, is constant over time, in agreement with the experimental observations [28]. In fact, the void fraction can be expressed through a dimensionless variable $\xi = x/\bar{\eta}(t)$ and it is the average of $\bar{\alpha}_c$ over ξ that is constant. As a result, the momentum balance equation intervenes only in the form of an instantaneous equation.
(3) Following Wedekind and Bhatt, the mean heat flux density $\bar{\varphi}_c$ exchanged between the fluid and the condenser wall could be assumed uniform and constant; the heat transfer coefficient is determined by the condenser design. This is a strong hypothesis for the model, which implies that the void fraction varies linearly along the two-phase zone.
(4) The viscous dissipation and the effects of axial conduction are negligible in the energy balance.
(5) The effects of compressibility in the vapor phase are such that ρ_v can be considered as uniform throughout the volume upstream of the condenser and in the two-phase zone [21].

The condenser can thus be divided into three zones (Fig. 4), governed by mass, energy and momentum equations:

• A compressible vapor zone, upstream of the condenser, of fixed length $L_{c,v}$, characterized by a variation of the mass flowrate from $\dot{m}_{c,i}$ at the condenser inlet to $\dot{m}^*_0$ at the beginning of the two-phase zone, and whose density varies according to the balance:

$$L_{c,v} S_c \frac{d\rho_v}{dt} = \dot{m}_{c,i} - \dot{m}^*_0 \tag{13}$$

Furthermore, it can be assumed that the vapor phase behaves as a perfect gas and that condensation is isothermal.

• A two-phase zone of variable length $\bar{\eta}(t)$, along which the flowrate changes from $\dot{m}^*_0$ to $\dot{m}^*_\eta$ and whose mass balance can be expressed by:

$$\rho_l(1-\bar{\alpha}_c) S_c \frac{d\bar{\eta}}{dt} + \bar{\alpha}_c S_c \frac{d(\rho_v \bar{\eta})}{dt} = \dot{m}^*_0 - \dot{m}^*_\eta \tag{14}$$

The energy balance in this zone is given by:

$$\rho_l(1-\bar{\alpha}_c) S_c \bar{h}_l \frac{d\bar{\eta}}{dt} + \bar{\alpha}_c S_c \bar{h}_v \frac{d(\rho_v \bar{\eta})}{dt} = -\bar{\varphi}_c \pi D_{h,c} \bar{\eta} + \bar{h}_l \dot{m}^*_0 - \bar{h}_v \dot{m}^*_\eta \tag{15}$$

where $\bar{h}_l$ and $\bar{h}_v$ are the mean specific enthalpies of liquid and vapor phases.

The frictional losses in the two-phase zone (steady momentum balance) are given by a complex relation such as:

$$p_{c,i} - p^*_\eta = f(\bar{\eta}, \dot{m}^*_0, \dot{m}_{c,o}) \tag{16}$$

• A liquid zone of variable length $\bar{\beta}(t)$, related to $\bar{\eta}(t)$ by a closure relation:

$$\bar{\beta}(t) = L_c - \bar{\eta}(t) \tag{17}$$

and obeying the mass balance:

$$\rho_l S_c \frac{d\bar{\beta}}{dt} = \dot{m}^*_\eta - \dot{m}_{c,o} \tag{18}$$

and the momentum balance:

$$\frac{\mathrm{d}\dot{m}_{\mathrm{c,o}}}{\mathrm{d}t} = \frac{S_{\mathrm{c}}(p_{\eta}^{*} - p_{\mathrm{c,o}})}{\bar{\beta}} \tag{19}$$

We thus obtain a system of equations with eight variables ρ_{v}, $p_{\mathrm{c,i}}$, $\dot{m}_{\mathrm{c,i}}$, $\bar{\eta}(t)$, $\dot{m}_{\eta}^{*}$, p_{η}^{*}, $\bar{\beta}(t)$ and $\dot{m}_{\mathrm{c,o}}$.

The matching of the numerical condenser model with the other parts of the fluid loop is achieved by means of the variables $\dot{m}_{\mathrm{c,i}}$ and $p_{\mathrm{c,o}}$ observed at the two condenser ends.

4.3. Model of liquid lines

The working fluid is transported between the various constituents of the system by three liquid lines as shown in Fig. 3: condenser-to-tee, evaporator-to-tee, reservoir-to-tee.

The hypotheses used concerning the liquid line flow are the following:

(1) the liquid is considered to be incompressible,
(2) the frictional pressure losses are negligible in comparison with the inertial effects.

The dynamic aspects of flow in the lines can then be described by means of a stationary model of pressure drop connecting the pressures and the flowrate between two arbitrary sections noted 1 and 2.

$$p_1 - p_2 = \lambda \frac{L}{D_{\mathrm{h}}} \frac{\dot{m}^2}{2\rho S} \tag{20}$$

where the friction factor λ is given by Colebrook's correlation:

$$\frac{1}{\sqrt{\lambda}} = -2\log_{10}\left(\frac{k}{3.71 D_{\mathrm{h}}} + \frac{2.51}{Re\sqrt{\lambda}}\right) \tag{21}$$

The thermal exchanges between the lines and the environment and those that develop between the reservoir and the condenser are taken into account: the heat transfers between the line walls and the outside thermal atmosphere are taken into account by means of a uniform heat transfer coefficient h_{la} determined by experiment. The energy balance of the flowing fluid is determined by considering the ratio between energy transported by advection and energy exchanged by conduction through the local Peclet number (i.e. the associated numerical scheme is a central-difference scheme if $Pe < 2$ and an upwind scheme otherwise). Thus, for lines discretized into n segments, coupled equations can be established giving the mass flowrates ($\dot{m}_{\mathrm{r}}$, $\dot{m}_{\mathrm{c}}$ and $\dot{m}_{\mathrm{e}}$), the pressures (p_{T} and $p_{\mathrm{e,i}}$ liquid pressure at the evaporator inlet) and the temperatures (T_{l_i}), in all the line volumes defined.

4.4. Model of vapor line

The vapor contained in the line connecting the evaporator with the condenser is considered to be incompressible and isothermal. The numerical model related to it calculates the pressure drop and the pressure p_{v_i} at various locations along this line, on the same principle as that for the liquid lines. In this element, one phenomenon has not been taken into account: the presence of liquid in the transport line connecting the evaporator with the condenser, which is considered in the model as occupied only by a vapor phase. As will later be seen, this aspect plays a fundamental role in the starting up phase.

4.5. Reservoir model

The control reservoir, in thermal contact with a thermally controlled tank and able to hold a large part of the working fluid mass, contains a free liquid–vapor interface where exchanges take place unceasingly. As already mentioned, it plays a fundamental role in the stability of the loop regimes and the physical numerical model should report these aspects in a most detailed way. The hypotheses used in this essential component of the system are the following:

(1) The liquid and the vapor are considered incompressible.
(2) The liquid–vapor interface at thermodynamic equilibrium is governed by the Clausius–Clapeyron equation (hypothesis verified by experiment).
(3) Both fluid phases present in the reservoir can be considered to be at saturation temperature T_{r}^{*}.
(4) Because of its horizontal cylindrical geometry, the reservoir volume occupied by the liquid is given by $\Omega_{\mathrm{r,l}} = L_{\mathrm{r}} S_{\mathrm{r,l}}$, where $S_{\mathrm{r,l}}$ depends on the liquid level $H_{\mathrm{r,l}}$ by a non-linear relationship.
(5) The kinetic energy and the viscous dissipation of the liquid and vapor phases are considered negligible in comparison with the exchanges by latent heat of vaporization and by conduction. The liquid and vapor internal energies are supposed to depend only on temperature.
(6) The convective exchange between the reservoir wall and the thermally controlled tank is sized by a heat transfer coefficient h_{tr}. The value is deduced from experimental results [29].

The resulting state variables calculated through the balance equations and the instantaneous transfer laws in the reservoir model are the height of the liquid contained $H_{\mathrm{r,l}}$, the fluid temperature T_{r}^{*} for both phases, the pressure reigning at the liquid–vapor interface p_{r}^{*}, and the reservoir inlet pressure $p_{\mathrm{r,i}}$. The control volumes in the

liquid and vapor phases and the associated state variables are presented in Fig. 3.

The variation of the liquid height in the reservoir is governed by the following equation:

$$\frac{\partial H_{r,l}}{\partial t} = \frac{\dot{m}_{r,i} - \overbrace{(S_r - S_{r,l})L_r\rho_v\left(\frac{l_v}{rT_r^*} - 1\right)\frac{\partial T_r^*}{\partial t}}^{[C]}}{L_r\left(\frac{\partial S_{r,l}}{\partial H_{r,l}}\right)(\rho_l - \rho_v)} \tag{22}$$

By scale analysis, it can be shown that the second term [C] in the numerator is negligible compared to the first term. The quantity of fluid exchanged by vaporization or condensation at the liquid–vapor interface of the reservoir is indeed negligible (in the ratio ρ_v/ρ_l) compared to the hydrodynamic contributions $\dot{m}_{r,i}$.

The vapor-phase pressure p_r^* is assumed to be equal to the saturation pressure corresponding to the temperature T_r^* of the liquid–vapor interface. It varies instantaneously with the state variables correlated by Clausius–Clapeyron's law:

$$p_r^* = p_0 \exp\left(-\frac{l_v M}{R}\left(\frac{1}{T_r^*} - \frac{1}{T_0}\right)\right) = p_{sat}(T_r^*) \tag{23}$$

The reservoir inlet pressure $p_{r,i}$ is obtained by combining momentum balance for liquid phase in the reservoir and momentum balance of liquid in the line connecting reservoir inlet to the Tee. Tedious derivation yields the following cumbersome relation:

$$p_{r,i} = \frac{\frac{H_{r,l}S_{rT}}{L_{rT}S_{eq}(1-\rho^+)}(p_T - \rho_l g\,\Delta H) + \frac{\dot{m}_{r,i}^2 F_2(\rho^+)}{\rho_l(S_{eq}(1-\rho^+))^2} + \rho_l g H_{r,l} + p^*\frac{S^*}{S_{eq}}}{\frac{S_{rT}}{S_{eq}} + \frac{H_{r,l}S_{rT}}{L_{rT}S_{eq}(1-\rho^+)}} \tag{24}$$

where $F_2(\rho^+)$ is a second order polynomial function of ρ^+, and where the symbol S_{eq} stands for $L_r\frac{\partial S_{r,l}}{\partial H_{r,l}}$.

The temperature of the liquid and vapor phases contained in the reservoir depends greatly both on the temperature and flowrate of the liquid entering the reservoir ($T_{r,i}, \dot{m}_{r,i}$) and on thermal exchanges with the thermostat temperature T_0. Combining balance equations leads to the following equation governing the variation of the temperature T_r^* in the reservoir:

$$\begin{aligned} &L_r\left[\rho_l c_l S_{r,l} + \rho_v c_v(S_r - S_{r,l}) + (S_r - S_{r,l})\rho_v\frac{l_v}{T_r^*}\left(\frac{l_v}{rT_r^*} - 1\right)\right]\frac{\partial T_r^*}{\partial t} \\ &\quad = \left(c_l(T_r^* - T_{r,i}) + \frac{p_{r,i} - p_r^*}{\rho_l} + \frac{\rho_v}{\rho_l - \rho_v}l_v - gH_{r,l}\right)\dot{m}_{r,i} \\ &\qquad - h_{tr}S_{tr}(T_r^* - T_l) + \varphi_l \end{aligned} \tag{25}$$

In the last two terms, (i) is the convective exchanges between the thermostat and the reservoir and (ii) the heat transfer between the immersed part of the line and the tank.

4.6. Complete loop model

Finally, the previous mathematical model for the two-phase loop appears as a large set of differential equations for state variable changes and algebraic transfer laws connecting physical objects of very diverse kinds. Inside the submodels needed to describe the system, there are small number of parameters or initial or boundary conditions ($\bar{\varphi}_c, h^*, h_{tr}, \bar{\eta}(0), H_{r,l}(0)$). Some of them could be correctly determined by means of an experimental evaluation, such as the mean heat flux $\bar{\varphi}_c$ at the condenser, the initial location of the liquid/vapor interface $\bar{\eta}(0)$ at the condenser and the initial height of liquid $H_{r,l}(0)$ in the reservoir. The parameter h^* remains difficult to estimate, so we have chosen a value which is generally accepted by other authors based on experimental results. Finally, by fitting simulations and experimental data, we determinated the parameter h_{tr}, whose role is crucial in the transient phases.

As a matter of fact, all the balance and transfer equations resulting from connecting the various elements of the system, have been expressed by means of the transfer evolution formalism (TEF) [30]. They are integrated into the modular software ZOOM and solved numerically in order to provide simulation data. In its current version, the numerical model of the CPL-type whole loop contains about forty modules of various types including 200 different state variables or transfer variables.

5. Experimental procedure

The range of applied powers that our device can evacuate "in a satisfactory way" at steady state depends strictly on the geometrical scaling and on the physical properties of the fluid. The vaporization enthalpy l_v, and the surface tension σ of the working fluid determines a range of working temperatures in the vicinity 30 °C [31], which establishes the reference temperature T_0 imposed by the thermally controlled tank which surrounds the reservoir. The qualification of "satisfactory or not" for the steady regime is made by taking into account both the parameters measuring the heat transfer efficiency of

the loop (overall heat transfer coefficient, mass flowrate) and the established regime characteristics (presence or not of shock waves or drafts, weak or strong amplitude fluctuations of the determining physical variables).

The application of a nominal heat load to the evaporator jacket, and the possible power steps which may be applied afterward, should be taken in relation with the parameters for optimal steady operation conditions ($T_w \simeq 30$ °C, $p \simeq 7$ bar). We were able to start-up the loop with small heat loads [31], and the maximum power that can be applied to the evaporator depends on the ability of the porous structure of the wick to resist deterioration caused by temperatures, in excess of 80 °C, the maximum possible for the wick which is made of polyethylene. In the present study, a nominal heat load of 200 W has been applied.

The initial conditions applied to the test loop are the following: the initial liquid height $H_{r,l}$, in the reservoir is 1.5 cm, the ambient temperature is 23 °C, the reservoir temperature T_r^*, equal to the temperature T_0 of the thermally controlled water tank, is 26.9 °C and the temperature of the liquid phase leaving the condenser is lowered to 9 °C by water cooling. The heat flux density evacuated at the condenser is 0.91×10^4 W m^{-2} and the absolute pressure in the reservoir p_r^*, corresponding to the saturation temperature T_r^*, is 6.96 bar.

Here, we consider the circumstances representative of the demands made on CPLs in various nominal situations, such as after an abrupt application or interruption of heat input due to the operation of power electronics. In this case, the whole fluid loop apparatus is arranged in the same horizontal plane and a power of 200 W is first applied to the evaporator. Steady running is established after 20 min or so. The power is then raised abruptly to 400 W (at $t_1 = 1100$ s). This power remains applied for 10 min, then lowered abruptly from 400 to 200 W (at $t_2 = 1700$ s). These power rise and fall simulate real situations of heat load cycling.

6. Comparative analysis of the loop behavior in response to power steps

Our concern here is with the characterization and descriptive analysis of these dynamic regimes.

Two working loop regimes deserve particular attention: the steady regime as established after application of a constant heat load to the evaporator, and the transient responses observed during sudden application or shutdown of power in the evaporator.

As evoked previously, it is necessary to insist on the fact that the priming transients have been simulated with initial conditions which are very different from reality. The assumption used to initiate simulation is that grooves in the metallic body of the evaporator and vapor line contain vapor. In the real conditions, the energy stored in the vapor phase which rises within the evaporator must be capable of pushing the liquid up towards the reservoir and the condenser, so as to establish a two-phase free interface in the condenser. This imposes a large initial temperature and pressure increase in the evaporator and a starting up phase faster than that simulated by the model. As an example, the curve of $p_r^*(t)$ to which we shall return, allows us to compare the difference of response which exists during the starting up between the experimental device and the simulations given by the model. So, for a time of less than a minute, simulation data cannot in any valid way be compared to those obtained by experiment. On the other hand, once the starting up phase is finished, the behavior is the same, as will be demonstrated in the curves shown in the next figures.

6.1. Loop behavior near steady-state operation

By comparing the simulations and the experimental data it can be noticed however that the permanent state is described in a very satisfactory way by the model: after a period of establishment common to most of them, the simulated and measured physical variables reach the same permanent mean value (Fig. 5). As an example, the pressure in the reservoir becomes established in its permanent value after about 850 s in the experimental device, while the model early gives a stabilization of p_r^*. This agreement at the permanent regime is a significant result, as far as the permanent state given by the model is insensitive to the fitting of crucial system parameters such as the thermal coefficients of exchange $\bar{\varphi}_c$, h^*, h_{tr}.

As seen in Section 1, various theoretical studies have shown that pressure oscillations are an inherent feature of CPLs steady operation. During the steady-state regime, two experimental variables present strongly fluctuating behavior, related to the instable phenomena accompanying the heat and mass transfer mechanisms at the liquid–vapor interfaces: the temperature T_r^* of the fluid in the reservoir and the pressure difference Δp_e at the evaporator ends. The origin of these high frequency oscillations is not clearly identified. We will show at a later stage how the oscillations increase during power steps and lead to overshoots or undershoots.

6.2. Description of mechanisms observed in the loop during the application of steps

The following two paragraphs describe the behavior of the system during the application of power steps:

- A sudden increase of the thermal load applied to the evaporator provokes an increase of the mass rate of the vapor phase. The increase of this vapor mass to be condensed entails a rapid increase of the length

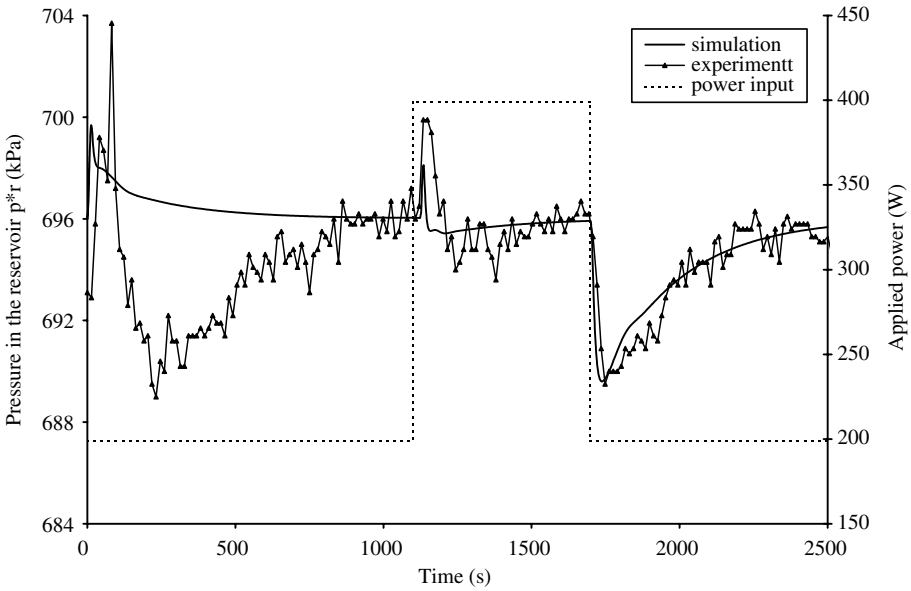

Fig. 5. Comparison between numerical and experimental data: pressure p_r^* in the reservoir.

of the two-phase zone in the condenser. The stage of growth of this two-phase zone is translated by a momentary increase of the liquid mass rate at the condenser outlet (overshoot). During the overshoot, the mass rate is much greater than the amount which has to enter into the evaporator in order to absorb the thermal load. As a consequence, the overshoot must be absorbed for its most part, by the reservoir.

- The global behavior of the loop is symmetric when a sudden decrease of the thermal load is applied to the evaporator. The rough decrease of the mass rate of vapor provokes such a rough decrease of the two-phase length in the condenser and, until this zone is again stable, a decrease in the liquid mass rate at the condenser outlet (undershoot). The liquid mass rate supplied by the condenser thus serves momentarily to feed the evaporator and it is the reservoir which, by emptying partially, counterbalances the failure of the later.

Let us now proceed to a precise analysis of the phenomena which take place in each of the loop elements, and their consequences on the global performance of the device.

6.3. Comparative analysis at reservoir level

We propose a comparison between the response of the experimental device and the behavior resulting from simulations for some of the characteristic dynamic regimes of CPL operating situations.

6.3.1. Comparative analysis in response to power steps

When the heat load increases from 200 to 400 W (at $t_1 = 1100$ s), the pressure and temperature variations ($p_r^*, T_{r,i}, T_r^*$) observed in the simulation results and in the experimental data present globally the same behavior (Figs. 5 and 6a and b). Notice in Fig. 5 that the increase of vapor pressure in the reservoir which follows the application of the power step is much greater for the experimental values (about 4 KPa) than for the simulations (almost multiplied by 2). This increase of 4 KPa of the pressure in the reservoir, much higher than the pressure losses (which are of the order of some hundreds of Pa), is echoed throughout the loop. It leads to an overshoot of the saturation temperature estimated at 0.2 K.

As stated previously, only parameter h_{tr} is used for fitting simulations and experiments, so as to preserve the physical approach of the CPL behavior. Its register is limited to the interval [100–200 $W m^{-2} K^{-1}$]. Given the importance of the risks encountered during the undershoots, it is preferable to adjust h_{tr} so that there is a good agreement during the downward step. It can thus be seen in Fig. 5 that beyond the downward step at 1700 s, there was a good agreement both for the undershoot amplitude and for time of returning of p_r^* to its steady value (low frequency damping).

When the power decreases from 400 to 200 W (at $t_2 = 1700$ s), the liquid level in the reservoir falls by about 0.5 cm. The outflow of liquid from the reservoir causes some of the liquid it contains to evaporate and leads to a lowering of the reservoir temperature and

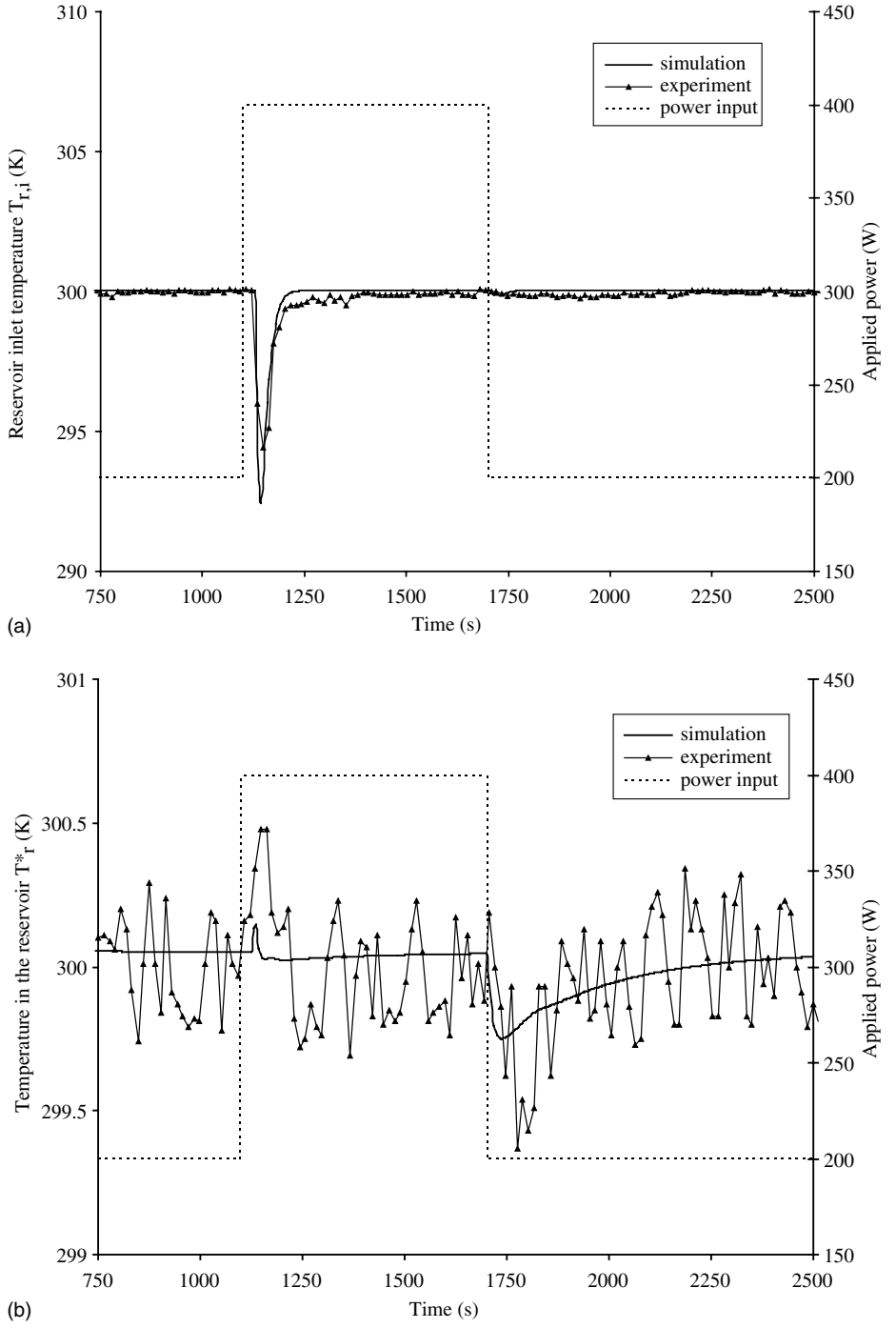

Fig. 6. Comparison between numerical and experimental data: temperatures $T_{r,i}$ and T_r^* at the inlet and in the reservoir.

pressure. This will always be the case since, when liquid leaves the reservoir (with a large thermal inertia), only the effects related to the vaporization of this liquid amount are to be taken into account; the heat necessary for this vaporization is at first taken from the liquid–vapor system, whose temperature decreases. For the reservoir inlet temperature $T_{r,i}$, thermal balance is re-established at T_0 after about 1 min (Fig. 6a). The vapor pressure in the reservoir returns to its reference value after a longer time (10 min) (Fig. 5).

6.3.2. Thermal and thermodynamic mechanisms

An interpretation from primary mechanisms, directly related to the most immediate phenomena, can be proposed. As mentioned previously, T_r^* seems to exhibit a response directly related to the $H_{r,l}$ fluctuations, which are themselves due to the variations of the two-phase region length $\bar{\eta}(t)$ in the condenser, and in the flowrate fluctuations in the evaporator.

Any intake of liquid into the reservoir $+\Delta\dot{m}_{r,i}$ leads to a rise of liquid $+\Delta H_{r,l}$ and causes a temperature and pressure increase (of about 0.4–0.6 K for the temperature) following the compression and adiabatic condensation of vapor which stays at the saturation pressure. The time constant of this reaction to a liquid intake is very small in comparison with the time constants of the conductive and convective phenomena of formula (25); the phenomenon is almost instantaneous. But this liquid intake from the condenser is an intake of cold liquid. If the reservoir liquid is supposed to be mixed by convection, the temperature can be expected to fall gradually, resulting in a reduction of the thermodynamic equilibrium temperature of the reservoir, i.e. of the reservoir vapor temperature T_r^*, which thus approaches the reference temperature imposed by the thermally controlled tank.

So, when liquid enters into the reservoir, the behavior of liquid level $H_{r,l}$, and indirectly T_r^*, results from a competition between the heat transport of cold liquid and the heat released by vapor condensation induced by the pressure increase due to the sudden intake of liquid.

6.4. Comparative analysis at evaporator level

6.4.1. Surface temperature of evaporators

For variations over time of T_s, Fig. 7 shows good agreement between calculated and measured values. This result is important as it proves the satisfactory behavior of the vaporization interface submodel within the global numerical model. The heat load is indeed absorbed in the same way as in the experimental device. The influence of the reservoir reactions is visible during the heat load transients: the damped oscillations (between 1300 and 1700 s) visible in Fig. 7 are imposed by the reservoir pressure variations (Fig. 5) analyzed previously. This illustrates the fact that the reservoir "imposes its working temperature" on the whole device. The absence of a peak following the increase of heat power (at $t = 1125$ s) in the temperature given by the numerical model is the consequence of the hypotheses on which the evaporator model is based (constant global heat transfer coefficient and vaporization interface fixed at the wick external surface).

6.4.2. Pressure at the evaporator ends

The comparison between theoretical and experimental results (Fig. 8) shows a noticeable difference for the dynamic behavior of the evaporator. The numerical model is not designed to reproduce the high frequencies of the moderate pressure oscillations (±200 Pa) observed experimentally. The unexplained gap between the experimental average Δp_e and the simulation results is also

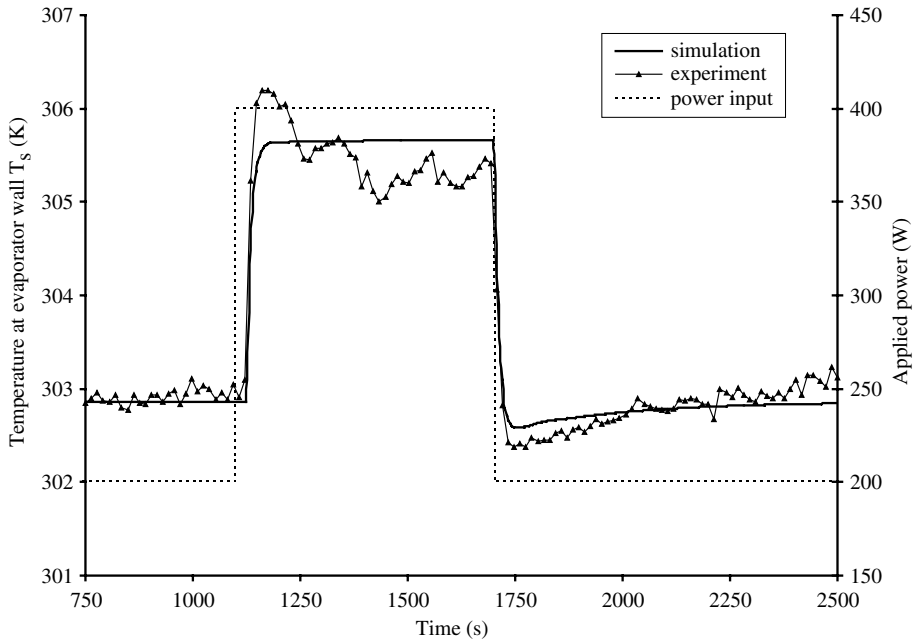

Fig. 7. Comparison between numerical and experimental data: mean temperature at the evaporator wall.

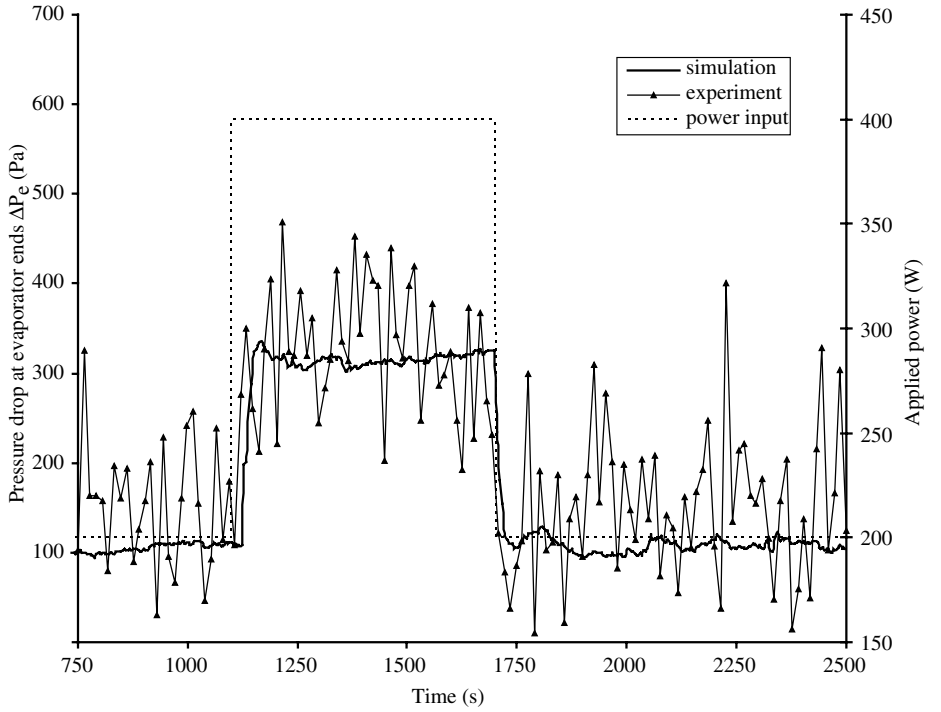

Fig. 8. Comparison between numerical and experimental data: pressure difference Δp_e at the evaporator ends.

noteworthy. The period of these oscillations is a few seconds (the measurement frequency is much higher than 1 Hz and does not allow the real frequency of these pressure oscillations to be measured). This cannot be reproduced at all by the numerical model.

During tests, it can be observed that the liquid level in the reservoir oscillates for a few millimeters, which is an amplitude that is completely compatible with the pressure oscillations measured at the evaporator ends. This liquid level fluctuations induce a pressure variation in the liquid phase, which affects both the free liquid/vapor interface location in the condenser and the presumed fixed liquid/vapor interface at the evaporator. The loop presents three liquid/vapor interfaces. According to the evaporator submodel hypotheses, the evaporator interface remains located at the wick surface. The two other interfaces (in the condenser and in the reservoir) are free interfaces, submitted to thermo-hydrodynamic instabilities.

As stated in the introducting section, the mechanisms capable of maintaining this type of oscillation, in which the amplitude depends largely on the operating regime of the loop, have not yet been clearly identified. None of these instability mechanisms are integrated in the present numerical model. Therefore, the numerical simulations cannot represent the pressure fluctuations, and the comparison between the pressure variation curves should be made through time averaging. The averaged variations Δp_e give values of the same order for the experimental data and the simulations. When the heat load is doubled from 200 to 400 W, Δp_e can be seen to increase from 150 to 350 Pa for the experimental data and from about 100–300 Pa for the simulations [32].

6.5. Comparative analysis at condenser level

It is not possible to make a direct comparison between experimental and numerical values. The numerical model gives a direct value of the two-phase zone length (Fig. 9a). On other part, diagram in Fig. 9b represents in particular the variation of temperatures T_{c2}, taken 1 m after the condenser inlet and T_{c3}, located near the end-of-condensation zone; these temperature variations present a fall down (undershoots at $t = 1700$ s for T_{c3} and at $t = 1800$ s for T_{c2}). These moved undershoots, observed immediately after a power step down, are due to the intrinsic behavior of the condenser, coupled with that of the reservoir; the various moments of temperature fall demonstrate a regression of the liquid/vapor interface towards the condenser inlet or so the variation of the two-phase zone length. Thus it can be seen that the value of this length, indirectly deduced from observation of sudden fall of the working fluid temperatures at various locations in the condenser, is confirmed by the model of the two-phase zone length.

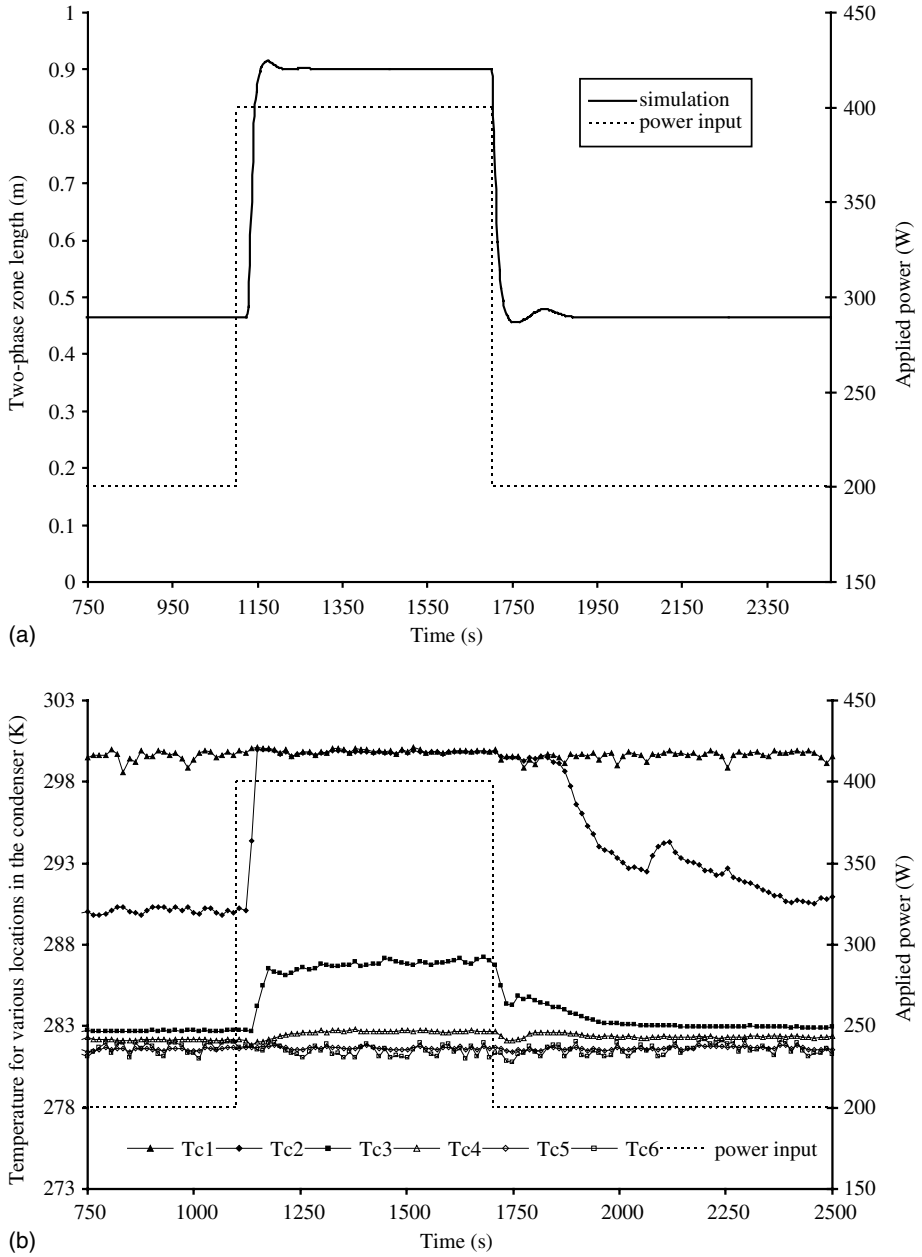

Fig. 9. Comparison between numerical and experimental data: (a) length of the two-phase zone and (b) temperatures in the condenser.

6.6. Comparative analysis of pressure effects at loop level

The analysis of the response to various imposed changes shows (Fig. 8) that the dynamic characteristics of the measured pressure values Δp_e (mean fluctuation amplitude, frequency) are sensitive to various loop control parameters such as the application of supplementary frictional losses (which reduce the fluctuation amplitude), and the power applied to the evaporator (the amplitudes of the initial overshoot and the fluctuations seem proportional to the power applied).

Furthermore, a comparison of the observations of Δp_e and Δp_c (pressure difference between the condenser ends) shows that, under the influence of the same types of constraints, the fluctuation amplitudes are greater (about double) at the condenser ends than at the evaporator ends. The previous observation encourages us to

suppose that the condenser is the source of the oscillations, which originate at its free interface [33].

These oscillations are damped within the loop both by the condenser–reservoir couplings and by friction inside the evaporator wick. Besides, the position chosen for the link between the reservoir and the loop has a certain influence on the regime of pressure oscillations Δp_e. This has been shown in theory and confirmed by

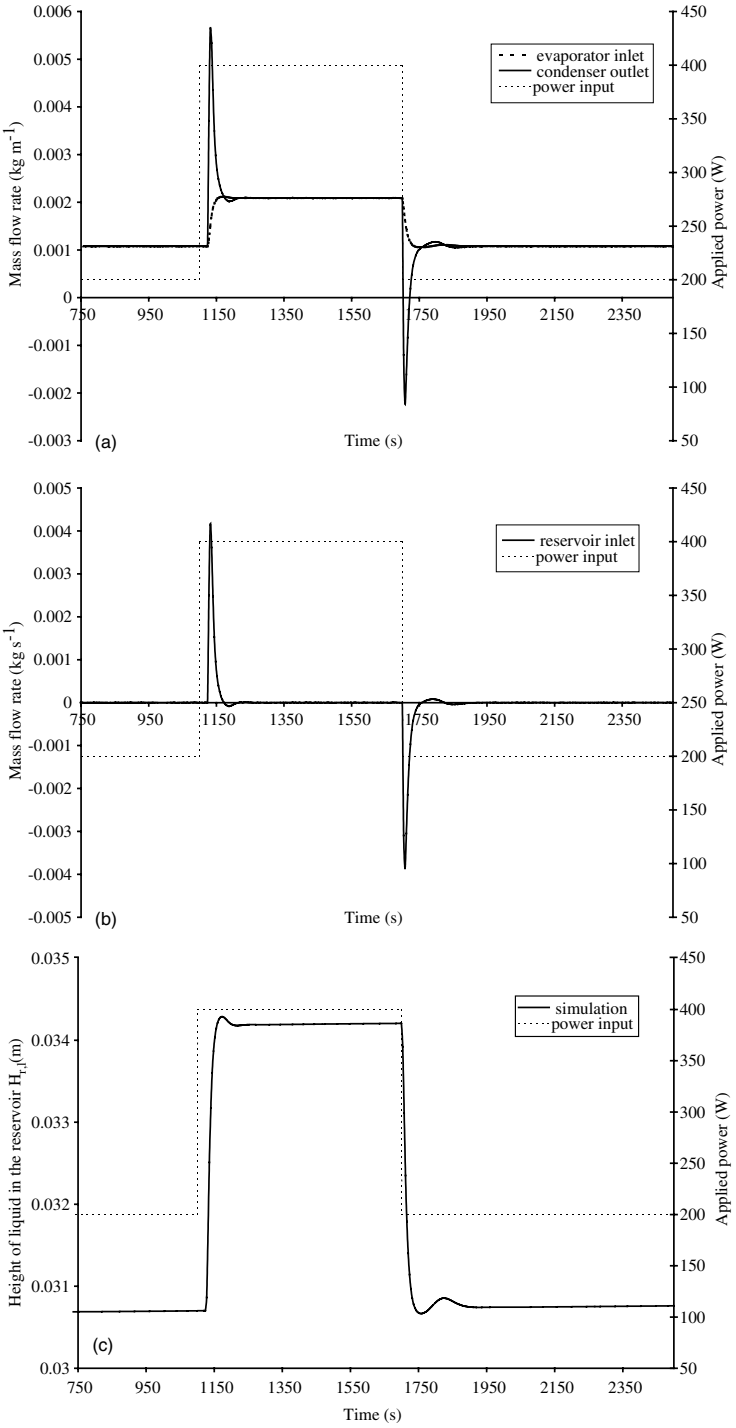

Fig. 10. Flowrate and liquid height variations in the reservoir (numerical results).

means of the condenser–reservoir coupling analysis [22]. This type of influence is made particularly clear by the variety of reservoir locations appearing in the early descriptions of CPLs published by research teams in the US.

6.7. Analysis provided by simulation

Numerous state variables followed by the numerical simulations cannot be the object of experimental measurements, either for reasons of accessibility (such as the internal temperature of the porous material T_w and the fluid it contains T_l, or the mean meniscus curvature $1/\bar{r}$), or because such measurements could considerably perturb the operation of the device, as for instance for flowrate measurements made by means of flowmeters which would generate pressure losses. However, variations over time of such unmeasured variables may be analyzed using simulation data.

6.7.1. Distribution of flowrates (Fig. 10)

When the applied power increases abruptly at instant t_1, the mass flowrate entering the evaporator also increases to reach the steady regime value in a monotonous way (Fig. 10a). The mass flowrate leaving the condenser also increases quickly and exceeds the value corresponding to the steady regime (causing an overshoot). This flowrate, which is much higher during transients, is the consequence of setting up a two-phase zone in the condenser. As previously shown, it causes liquid to enter in the reservoir (Fig. 10b), leading to an increase of the liquid height (Fig. 10c). Conversely, the reduction of the applied power at t_2 creates an inversion of the flow direction in the condenser, which causes an undershoot of the mass flowrate. The mass flowrate leaving the condenser falls momentarily below the value corresponding to the steady regime, the amplitude of the undershoot being such that the flowrate becomes negative at the condenser exit. At this precise moment, the reservoir, where a decrease in the liquid height can be seen, feeds the evaporator and the condenser simultaneously.

6.7.2. Behavior of the vaporization interface

When the heat load increases from 200 to 400 W, the difference between the temperature of the liquid under the meniscus and the temperature of the vaporization interface increases, which stabilizes the system behavior from a thermal point of view (Fig. 11a). Conversely, a heat load decrease entails a decrease of this temperature difference, making the system more thermally unstable.

Indeed, these temperatures can become very close (crossing of curves) if there is a very marked heat load decrease, which causes a very abrupt vaporization of the liquid in the depths of the wick. This entails a recession of the vaporization interface, a decrease of the overall transfer coefficient and thus a fall in the global performance of the capillary pump. But it can also entail a deterioration of the wick surface and irreversible draining of the device [34]. It is also noticeable that, in steady regime, the difference between the vaporization interface temperature and the reservoir temperature increases with the heat load (Fig. 11b and c). This increase is due to an increase in meniscus curvature ($1/r$), at the vaporization interface (Fig. 11b).

7. Simulated conditions of draining

This is a simulated case that cannot be verified by measurement because the heat load variation needed exceeds the capacities of our experimental apparatus and could seriously deteriorate the wick. The purpose of the simulated scenario is to show the role that the reservoir plays in the device response during large abrupt variations of the heat load.

The simulated scenario proceeds as follows: once the steady regime has been reached by application of a 500 W heat load to the evaporator, the applied power is abruptly decreased to 100 W (at the instant $t = 1000$ s). The averaged heat flux density $\bar{\varphi}_c$, evacuated by the condenser is then evaluated following the Wedekind model to 0.18×10^4 W m^{-2}.

When a step down of the heat power is suddenly applied to the evaporator, the simulation shows (Fig. 12) that the loop reaction is very sensitive to the amplitude of the power decrease. A drop of 400 W entails a reduction of the two-phase zone length (which quickly falls from 6 to 1 m) and a rapid intake of liquid from the reservoir, causing a 2.5 K decrease of its vapor temperature and a 50 KPa drop in its saturation pressure. The equilibrium temperature of the reservoir falls below the liquid temperature in the insulator, which can cause the liquid to boil in the line and drain the evaporator. This result is important because it shows that draining can be due to phenomena that take place far outside the active zones where the phase transitions generating instabilities should normally occur (i.e. in the evaporator and the condenser). It also shows the importance of the reservoir behavior in the global CPL response and the attention that should be paid to its sizing and its location between condenser and evaporator during the technological design phases.

8. Conclusion

One of our first objectives was to ensure that the global model of the CPL device we have developed reproduces correctly the behavior of these loops following steps of the applied thermal load. This purpose is

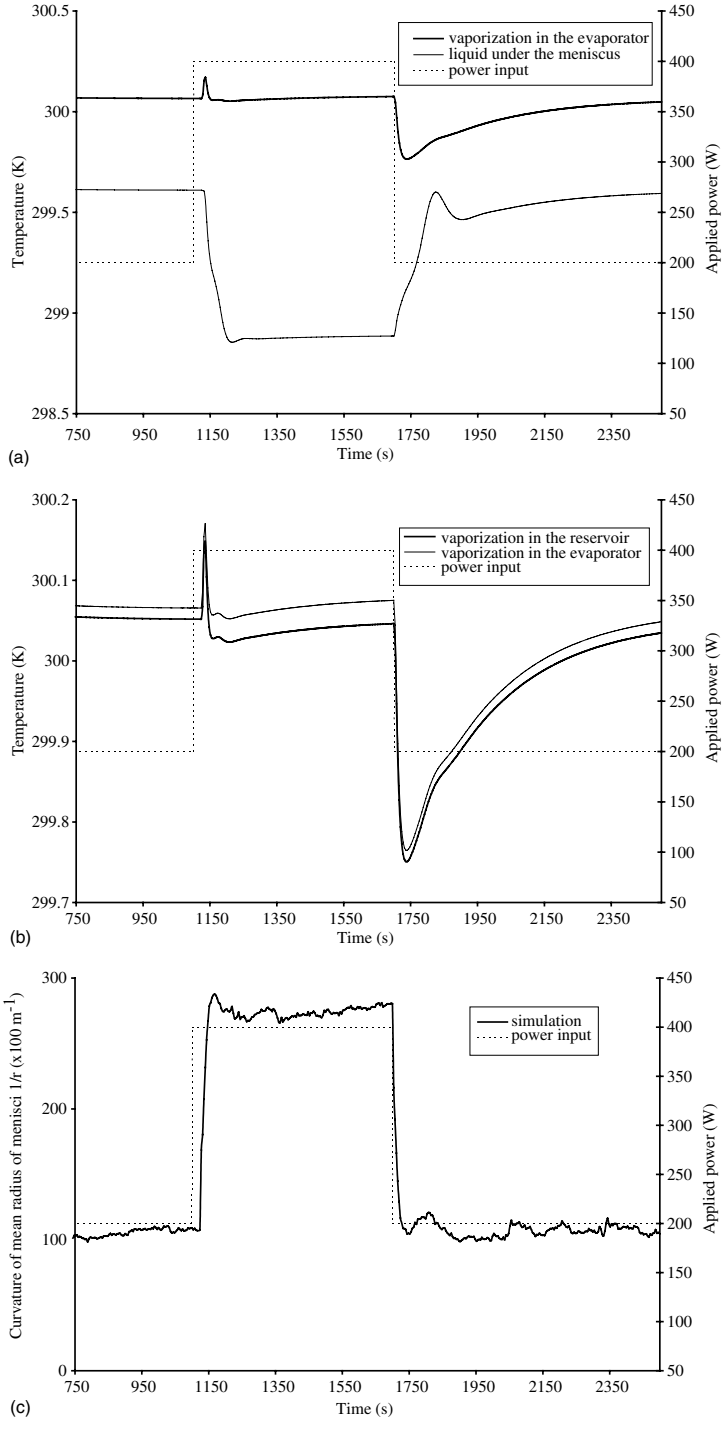

Fig. 11. Liquid–vapor interface behavior (numerical results).

a preliminary for any behavior analysis and has been achieved satisfactorily.

The self-sustained oscillations of higher frequencies are not reproduced by the model. These oscillations can result from a cyclic movement of the vaporization interface just under the wick surface (the very strong thermal resistance of these wicks, with the risk of destruction by fusion, prevents the vapor from

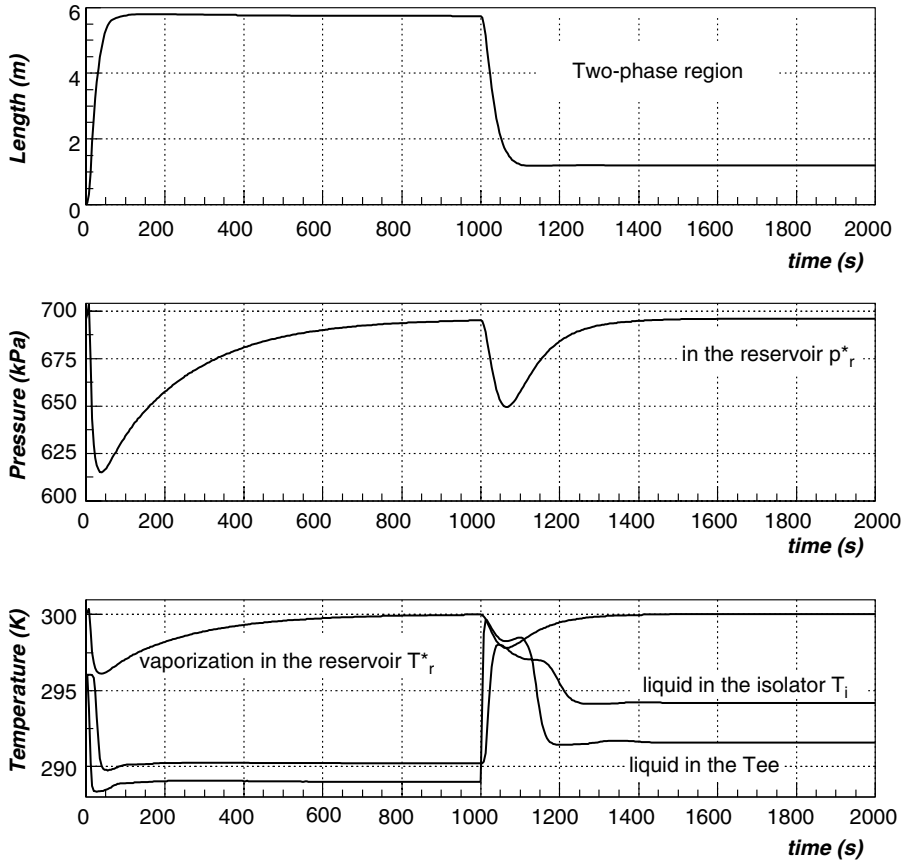

Fig. 12. Two-phase zone behavior after a power step down.

penetrating deeply there); these oscillations can also originate from the condenser. They are not reproduced however by the model of Wedekind.

Furthermore, the model/experiment comparisons presented prove that the condenser/reservoir coupling is at the heart of the mechanisms activating the abrupt variations of temperature and of pressure observed following the application of power steps. The analysis provides an explanation for the instabilities and for damped oscillations of low frequency observed between the condenser and the reservoir. These instabilities have also enabled us to explain why these devices react badly to abrupt decreases of applied power.

Appendix A. Main geometrical data of the experimental setup

Evaporator

- Porous wick—outer diameter: 19 mm; inner diameter: 12 mm; axial length: 210 mm; mean pore radius: 20 μm; $\kappa = 1.1 \times 10^{-12}$ m^2; $\varepsilon = 0.5$.
- Evaporator jacket—outer diameter: 36 mm; inner diameter: 19 mm; axial length: 240 mm (heated portion: 190 mm); groove diameter: 2 mm; $k_s = 132$ W m^{-1} K^{-1}.

Condenser

- Outer diameter: 16 mm; inner diameter: 14 mm; axial length: 6.6 m; fins outer diameter: 36 mm; cooling waterline inner diameter: 43 mm.
- Maximum cooling water flowrate: 256 l h^{-1}.

Fluid lines

- Vapor line—outer diameter: 16 mm; inner diameter: 14 mm; length: 3 m.
- Liquid line—outer diameter: 10 mm; inner diameter: 8 mm; rigid length: 3 m.

Reservoir

- Outer diameter: 100 mm; length: 230 mm; reservoir volume: 2.5 l (overall loop volume: 2 l).

Isolator

- Porous medium—inner diameter: 12 mm; outer diameter: 20 mm; length: 100 mm; mean pore radius: 60 μm; $\kappa = 3.3 \times 10^{-12}$ m^2; $\varepsilon = 0.5$.

Parameters

- Heat transfer coefficient at the vaporization interface: $h^* = 11\,000$ W m^{-2} K^{-1} (from experimental data).
- Heat transfer coefficient between liquid line working fluid and ambient air: $h_{la} = 8$ W m^{-2} K^{-1}.
- Heat transfer coefficient between reservoir working fluid and thermally controlled bath water: $h_{tr} = 100$ W m^{-2} K^{-1}.
- Characteristic time of heat load applied to the evaporator: $\tau = 10$ s (from experimental data).
- Heat transfer coefficient between working fluid and porous wick structure: $h_{lw} = 2000$ W m^{-2} K^{-1}.
- The mean heat flux density to be evacuated at condenser is evaluated by means of temperatures from various thermocouples located in the working fluid (T_{c1} to T_{c7}).

References

[1] K.P. Hallinan, J.S. Allen, Comments on the operation of capillary pumped loop devices in low gravity, in: 4th Microgravity Fluid Physics & Transport Phenomena Conference, Cleveland, OH, 1998.

[2] J. Ku, E. Kroliczek, D. Butler, R. McIntosh, Capillary pumped loop GAS and Hitchhiker flight experiments, AIAA Paper 86-1289, 1991.

[3] Y. Maidanik, Y. Fershtater, K. Goncharov, Capillary pumped loop for the systems of thermal regulation of spacecraft, in: 25th International Conference on Environmental Systems, SAE Paper, 1991.

[4] M. Nikitkin, B. Cullimore, CPL and LHP technologies: what are the differences, what are the similarities? SAE Paper 981587, 1998, pp. 400–408.

[5] J. Ku, Operating characteristics of loop heat pipes, SAE Paper 1999-01-2007, 1999, pp. 1–16.

[6] A. Delil, M. Dubois, W. Supper, TPX for in-orbite demonstration of two-phase heat transport technology-evaluation of flight and post-flight experiments results, in: 25th International Conference on Environmental Systems, SAE Paper 951510, 1995.

[7] A. Faghri, Heat Pipe Science and Technology, Taylor & Francis, Washington, 1995.

[8] S. Clayton, D. Martin, J. Baumann, Mars surveyor thermal management using a fixed conductance capillary pumped loop, SAE Paper 972467, 1997, pp. 899–910.

[9] T. Hoang, J. Ku, Hydrodynamic aspect of capillary pumped loop, SAE Paper 961435, 1996, pp. 1–5.

[10] D. Butler, L. Ottenstein, J. Ku, Design evolution of the capillary pumped loop (CAPL-2) flight experiment, SAE Paper 961431, 1996, pp. 1–13.

[11] C. Figus, Y. Le Bray, S. Bories, M. Prat, Heat and mass transfer with phase change in a porous structure partially heated: continuum model and pore network simulations, Int. J. Heat Mass Transfer 42 (1999) 2257–2599.

[12] Q. Liao, T.S. Zhao, A visual study of phase-change heat transfer in a two-dimensional porous structure with a partial heating boundary, Int. J. Heat Mass Transfer 43 (2000) 1089–1102.

[13] T.S. Zhao, Q. Liao, Rapid vaporization of subcooled liquid in a capillary structure, Int. J. Heat Mass Transfer 45 (2002) 165–172.

[14] J.S. Allen, K.P. Hallinan, Liquid blockage of vapor transport lines in low Bond number systems due to capillary-driven flows in condensed annular films, Int. J. Heat Mass Transfer 44 (2001) 3931–3940.

[15] L. Swanson, G. Herdt, Model of the evaporating meniscus in a capillary tube, J. Heat Transfer, Trans. ASME 114 (1992) 434–441.

[16] P. Stephan, C. Busse, Analysis of the heat transfer coefficient of grooved heat pipe evaporator walls, Int. J. Heat Mass Transfer 35 (1992) 383–391.

[17] Y. Cao, A. Faghri, Analytical solutions of flow an heat transfer in a porous structure with a partial heating and evaporation on the upper surface, Int. J. Heat Mass Transfer 37 (10) (1994) 1525–1533.

[18] A. Demidov, E. Yatsenko, Investigation of heat and mass transfer in the evaporation zone of a heat pipe operating by the 'invert meniscus' principle, Int. J. Heat Mass Transfer 37 (1994) 2155–2163.

[19] Y. Cao, A. Faghri, Conjugate analysis of a flat-plate type evaporator for capillary pumped loops with three-dimensional vapor flow in the groove, Int. J. Heat Mass Transfer 37 (1994) 401–409.

[20] R.B. Schweickart, L. Neiswanger, J. Ku, 22nd AIAA Thermophysics Conference, Honolulu, Paper AIAA 87-1630, 1987.

[21] B. Bhatt, G. Wedekind, Transient and frequency response characteristics of two-phase condensing flows: with and without compressibility, J. Heat Transfer, Trans. ASME 102 (1980) 495–500.

[22] O. Fudym, Modèle physique de fonctionnement d'une boucle fluide diphasique à pompage thermocapillaire. Etude de prototype et analyse de couplage, Thèse de Doctorat de l'Université Paul SABATIER, Toulouse, France, 1994.

[23] V. Platel, O. Fudym, C. Butto, P. Briend, Coefficient de transfert, à l'interface de vaporisation d'une boucle fluide diphasique à pompage thermocapillaire, Rev. Générale thermique 35 (1996) 592–598.

[24] J.-L. Joly, Méthodologies de modélisation, d'analyse de couplage et de sensibilité pour les systèmes énergétiques et les procédés. le formalisme d'evolution par transferts (T.E.F.) et le logiciel ZOOM, Thèse de Doctorat d'Etat, Université Paul SABATIER. Toulouse, France, 1998.

[25] V. Platel, C. Butto, J. Grandpeix, J.-L. Joly, Modèle d'évaporateur d'une boucle fluide diphasique à pompage capillaire, Rev. Générale Thermique 35 (1996) 434–449.

[26] J. Ku, E. Kroliczek, R. McIntosh, Analytical modeling of the capillary pumped loop, in: Proceedings of the 6th International Heat Pipe Conference, Grenoble, France, 1987.

[27] B. Bhatt, G. Wedekind, A self-sustained oscillatory flow phenomenon in two-phase condensing flow systems, J. Heat Transfer, Trans. ASME 102 (1980) 694–700.
[28] G. Wedekind, B. Bhatt, B. Beck, A system mean void fraction model for predicting various transient phenomena associated with two-phase evaporating and condensing flows, J. Multiphase Flow 4 (1978) 97–114.
[29] A. de Guilhem de la Taillade, Comportement du système liquide–vapeur dans le réservoir de commande d'une pompe thermocapillaire, Master's thesis, Université Paul SABATIER, Toulouse, France, 1996.
[30] J. Bonin, J. Grandpeix, J. Joly, A. Lahellec, V. Platel, M. Rigal, Multimodel simulation: the T.E.F. approach, in: Simulation Applied to Manufacturing Energy and Environmental Studies, Proceedings of ESM'89 Congress, Rome, Italy, 1989.
[31] V. Platel, C. Butto, O. Fudym, M. Laurens, Boucle fluide diphasique à pompage thermo-capillaire. Etude expérimentale du fonctionnement et évaluation des performances, Rev. Générale Thermique 34 (1995) 315–324.
[32] E. Pouzet, Conception et réalisation d'un prototype de boucle fluide diphasique à pompage thermocapillaire destiné à étudier l'influence du champ de pesanteur sur ces dispositifs, Thèse de Doctorat de l'Université Paul SABATIER, Toulouse, France, 1996.
[33] G. Wedekind, B. Bhatt, G. Roslund, An experimental and theoretical study of transient pressure drop in two-phase condensing flow, J. Heat Transfer, Trans. ASME 111 (1989) 546–551.
[34] M. McCab, J. Ku, S. Benner, Design and testing of a hight power spacecraft thermal management system, NASA technical memorendum 4051, 1988.